**TECHNISCHE
UNIVERSITÄT
DRESDEN**

Simulating Multi Layer Targets for Grazing Incidence Small Angle X-ray Scattering

vorgelegt von

Franziska-Luise Paschke-Brühl
geboren am 30.07.1999 in Dresden

Institut für Teilchen- und Kernphysik
Fakultät Physik
Bereich Mathematik und Naturwissenschaften
Technische Universität Dresden
2021

Summary

Abstract

English:

This bachelor thesis studies the feasibility of grazing-incidence small-angle x-ray scattering (GISAXS) in the UHI laser-target interaction via computational simulations with SMILEI. In this work we briefly analyze the front and back of the target. We find predominantly that the compression of the target becomes apparent in the GISAXS pattern, while we can not observe ablation. We will mainly focus on the density oscillation, a dynamic that has not been mentioned in literature yet. The density oscillation dynamics depend on a simple pressure gradient in between the layers. We observe the multi layers inversely oscillating in density and a global density alteration moving through the target. The density alteration allows to recognize the dynamic in a GISAXS pattern. We learn, that GISAXS is feasible in the high intensity regime, but not for the same dynamics as in the lower intensity regime.

Abstract

Deutsch:

Diese Bachelorarbeit befasst sich mit der Realisierbarkeit der Target Diagnostik "grazing-incidence small-angle x-ray scattering"(GISAXS) für den ultra-hohen Intensitätsbereich der Laser-Target Interaktion via Computer Simulationen in SMILEI. Zu Beginn wird kurz auf die Front- und Rückseite des Targets eingegangen. Wir sehen, dass nicht die Ablation, jedoch die Kompression, im GISAXS Profil erkennbar ist. Der Hauptteil der Arbeit befasst sich mit der Dichte Oszillation, eine Dynamik, die in Multilayer Targets auftritt und noch nicht in Literatur beschrieben wurde. Die Dynamik beruht auf einem simplen Druck-Unterschied zwischen den Layern im Target. Im Dichteprofil sieht man die Layer invers zueinander oszillieren und eine resultierende globale Dichte Veränderung, die sich durch das Target bewegt. Diese Dichte Veränderung erlaubt es der Dynamik im GISAXS Profil zu folgen. Wir lernen, dass GISAXS im ultra-hoch Intensitätsbereich anwendbar ist, aber andere Dynamiken sichtbar sind, als für niedrigere Intensitäten.

Contents

List of Figures

List of Tables

List of Abbreviations

GISAXS   grazing-incidence small-angle x-ray scattering

SAXS   small-angle x-ray scattering

GID   grazing incidence diffraction

CCD   charge-coupled device

UHI   ultra high intensity

TNSA   target normal sheath acceleration

RPA   radiation pressure acceleration

CSA   collisionless shock acceleration

HZDR   Helmholtz Zentrum Dresden-Rossendorf

ML   multi layer

RTI   Rayleigh-Taylor instability

DO   density oscillation

1 Introduction

This thesis investigates the dynamics of ultra-high intensity laser-target interaction via computational simulations. The goal is to either reason an application of GISAXS in this intensity regime or to advise against it.

Studying laser-target interaction is highly interesting for many reasons. The first is the creation of a plasma and the possibility to study it under different conditions. One can study for example heat transport in high density plasma for experiments regarding astrophysics [1] or thermonuclear fusion [2]. Here a terrestrial and relatively small experimental setup allows to learn about interstellar nebulae and fusion in stars. The second reason are the particle acceleration mechanisms one can study when a laser of significant intensity hits a solid target.

Laser-plasma acceleration is a relatively new alternative to large and costly linear accelerators and synchrotrons with a variety of applications such as medical physics [3], where tumors are treated with the ionizing radiation. Modern laser facilities are capable of laser intensities up to 10^{22} Wcm^{-2}, which allows electron energies in the MeV+ range, the record being 8 GeV [4]. Even the much heavier protons and ions can be accelerated to high energies, the record for proton energy and ultra-short laser pulses is 80 MeV [5].

When studying a plasma one can apply a number of diagnostics, for example Thomson scattering, a Faraday cup or a Langmuir probe. In this thesis we will concentrate on grazing-incidence small-angle scattering (GISAXS), which is based on the Thomson scattering of x-rays on the electrons in the plasma. The goal is to follow up on a recent publication about GISAXS [6]. The paper studies experiments and corresponding simulations, that apply GISAXS on multi layer structures, for laser intensities I = 10^{14}-10^{16} Wcm^{-2}. Modern laser facilities are capable of intensities of up to 10^{22} Wcm^{-2} and higher energies in the plasma cause relativistic effects, not apparent in lower energy plasma, but relevant for acceleration mechanisms. Therefore exceeding the intensities in the paper and applying GISAXS for I > 10^{16} Wcm^{-2} is of great interest. In this thesis we will investigate the feasability of GISAXS in the ultra-high intensity regime. The main questions are:

- What kind of physics can we observe in this intensity regime?

- Do the dynamics show in the electron density of the target in a way, that allows a GISAXS diagnostic to recognize it?

- What should an experimental setup look like?

The multi layer target and laser parameters correspond to the setup of [6]. We will use the evaluation of [6] as a reference throughout this work, trying to extend these studies to higher intensities. Nevertheless, own adaptions have been made in the target geometry to show the dynamics of the density oscillation.

The density oscillation is a dynamic occurring in a multi layer target, that will be described in the main part of this thesis. The dynamics have not been described before and are easy to understand with basic plasma physics. The goal is to study these physics but also show, that the UHI regime offers interesting dynamics that are recognizable in a GISAXS pattern. We will also briefly focus on the plasma expansion dynamics in order to follow up the theoretical studies of [6].

2 Theoretical Background

2.1 Grazing-incidence Small-angle X-ray Scattering

GISAXS is an analysis technique to characterize micro- up to nano-scale density correlations and to examine shapes of objects at their surface or buried interfaces. The x-ray beam is scattered on the electrons of the target, applying Thomson scattering. The electron density of the target determines the scatter pattern. For a multi layer target, the xray beam gets scattered on both layers, higher cross section for the layer with higher electron density. This creates a characteristic pattern, that allows to determine the position and width of the layers. GISAXS represents an extension of grazing incidence diffraction (GID) to small scattering angles, as well as a SAXS experiment implemented in a reflection scattering geometry. Facilities with a GID or SAXS beam line can be easily modified for GISAXS, by adding a precise goniometer and a 2D detector, e.g. a CCD detector. In the laboratory a focused and collimated x-ray beam is directed towards the target, a thin multilayer film supported on a flat substrate. A sample-tilt stage allows to control the grazing -incidence angle, i.e. the incidence angle of the x-ray beam, usually in the range of 0.05° - 0.5°. The beam is efficiently reflected off the target and hits the 2D detector. The general setup is shown in Figure (2.1).
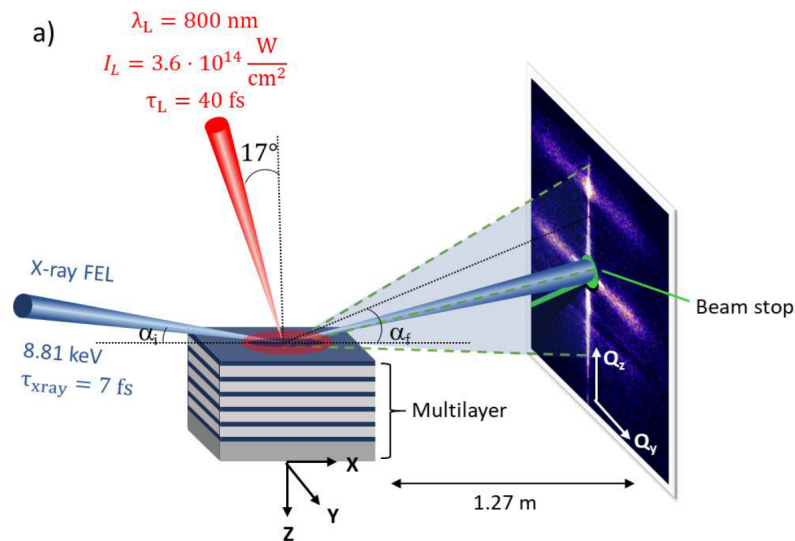
Figure 2.1: Laboratory Setup of a GISAXS diagnostic, as in [6].

The focused x-ray beam hits the target in a long stripe over the surface due the grazing-

incidence angle. This leads to a wide illuminated area, effectively increasing the scattering volume and causing the pattern to be statistically representative of the whole surface.

In order to recognize the layers in the pattern, the electron density difference between the layers has to be significant. In the reference setup [6], for example, the pattern is sensitive to layers that differ by at least 200 n_c in electron density, which denotes 2-3% of the highest electron density.

The peak structures in reciprocal space in the scatter pattern represent different aspects of the density profile in real space, e.g. the Bragg peak relates to the typical scale length of each double layer and the Kiessing fringes to the number of double layer repetitions in the target [6]. Figure 2.2 displays an example of a line out of in-plane scattering, showing the Bragg peak, Kiessing fringes and Yoneda peaks. The evaluation and quantitative analysis of the pattern can be done with BornAgain [8]. The open-source software can be used to simulate and fit x-ray and neutron reflectomery, off-specular scattering and GISAXS. Thereby giving access to the targets nano-scale density profile.
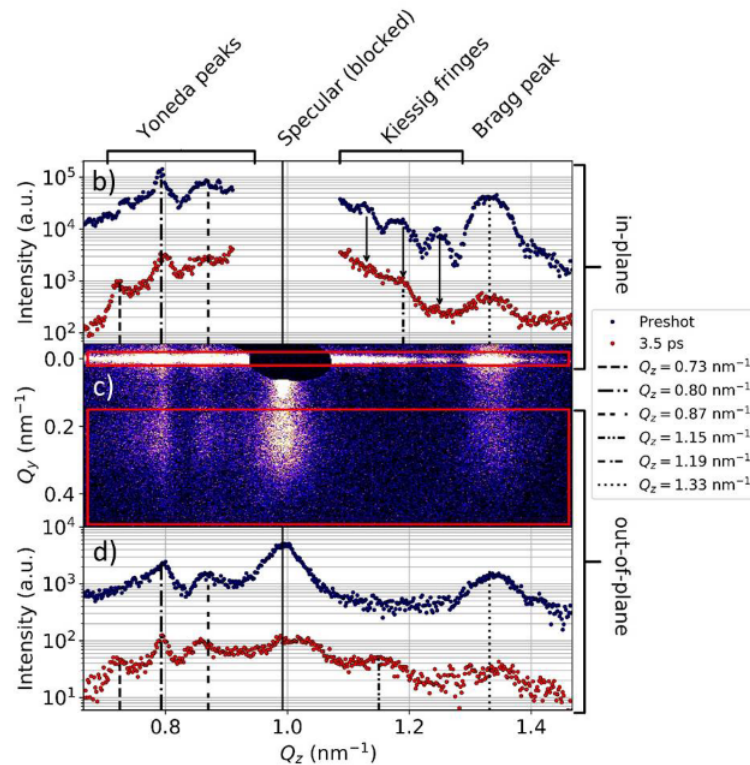
Figure 2.2: GISAXS scattering pattern of [6].

Because a simulation knows all its parameters, it is easy to access the density profile at any time. Here one has to do the inverse process as above, deriving the scatter pattern from the density profile in order judge whether a dynamic is recognizable in a GISAXS diagnostic. In this work we will only qualitative analyze the density profiles, but a next step would be to to calculate a GISAXS pattern based on the density profiles of the simulation. The pattern can

be created in BornAgain as well.

For this thesis we set two parameters to roughly judge whether we see an electron profile in the GISAXS pattern:

- density resolution $n_{GISAXS} = 200 \; n_c$: an electron density peak has to be at least 200 n_c high, to recognize it in the GISAXS scatter pattern

- time resolution $t_{GISAXS} = 500$ fs: the pattern and therefore the electron density profile can be taken every 500 fs

2.2 Target Dynamics

The interaction of the incident laser with the solid target causes a series of dynamics to occur in matter. To predict their nature and strength one should determine the regime they are operating in, e.g. laser energy range, geometry and density of the target. In this work we study a short pulse, ultra-high intensity laser hitting a solid density multi layer target. The underlying process for all dynamics below is the rapid ionization of ordinary matter when exposed to high intensity radiation. The released electrons are caught in the laser field and oscillate with a characteristic energy.

2.2.1 Heating and Melting

The absorption of laser energy leads to heating of the target. While classical heating describes the increase of the atomic kinetic energy directly via a momentum transfer, energy input by a laser only addresses the electrons of the system. This causes a transient non equilibrium of electrons and ions, i.e. the lattice, and is based on the enormous difference in mass of electrons and ions or respectively, difference in ion sound speed c_{si} and electron Fermi velocity v_f. The absorbed pulse energy is therefore stored in the electron subsystem while the lattice stays considerably colder. Lattice heating happens rather slow, with characteristic times for different metals being 1-100 ps [9]. It can be described by the electron-lattice relaxation, so the energy exchange between electrons and ions can be described as:

$$c_i \frac{\partial T_i}{\partial t} = -c_e \frac{\partial T_e}{\partial t} = \alpha(T_e - T_i)[9], \tag{1}$$

where T_i/T_e describe the temperature, c_i/c_e the specific heat and α the energy exchange rate between the two subsystems. Also i,e stand for ions and electrons, respectively. Another aspect of heating is the energy transfer from the hot surface to the cold bulk of the target. In metals the transport happens due to the electron heat conduction, but special cases require to take lattice heat conduction into account. This is described by the energy transport equation of a

collisional plasma by Nicholas[23, 10]:

$$\frac{\partial \epsilon}{\partial t} + \nabla \cdot (\mathbf{q} + \mathbf{\Phi}_a) = 0, \tag{2}$$

where $\epsilon = c_e T_e$ is the energy density, $\mathbf{q}(x) = -\kappa_e \nabla T_e$ the Spitzer-Härm heat-flow [11] and $\mathbf{\Phi}_a = \eta_a \mathbf{\Phi}_L$ the absorbed laser flux. Including (1), one gets the two-temperature energy conversation equations:

$$\begin{aligned} c_e \frac{\partial T_e}{\partial t} &= \nabla(\kappa_e \nabla T_e) - \alpha(T_e - T_i) + Q \\ c_i \frac{\partial T_i}{\partial t} &= \alpha(T_e - T_i), \end{aligned} \tag{3}$$

where $Q = \nabla \Phi_a$ for 1D is the power density deposited by the laser and $\kappa_e(\nu_{ei})$ the Spitzer heat conductivity. The energy exchange rate can be described by $\alpha = c_i/\tau_i$ with the characteristic time of lattice heating $\tau_i = m_i/(2m_e \nu_{ei})$, m_e and m_i the mass of electrons and ions. The electron-ion collision frequency after Spitzer is

$$\nu_{ei} \simeq 2.91 \times 10^{-6} Z n_e T_e^{-3/2} \ln\Lambda \quad s^{-1} [23]. \tag{4}$$

Here Z denotes the number of free electrons per atom, n_e is the electron density in cm^{-3} and $\ln\Lambda$ is the Coloumb logarithm for the limits $b_{\max}$ and $b_{\min}$ of the electron-ion scattering cross-section:

$$\Lambda = \frac{b_{\min}}{b_{\max}} = \lambda_{\mathrm{D}} \frac{k_B T_e}{Z e^2} = \frac{9 N_D}{Z}, \tag{5}$$

where

$$\lambda_{\mathrm{D}} = \left(\frac{k_B T_e}{4\pi n_e e^2}\right)^{1/2} \tag{6}$$

is the Debye length and

$$N_{\mathrm{D}} = \frac{4\pi}{3} \lambda_{\mathrm{D}}^3 n_e \tag{7}$$

is the number of particles in a Debye sphere [23].

Neglecting the electron-lattice relaxation in (3) and following Rozmus and Tikhonchuk [12], like in [23], one can derive the heat front position

$$x_f \simeq 65 \left(\frac{n_e}{10^{23}\mathrm{cm}^{-3}}\right)^{-7/9} Z^{-2/9} \left(\frac{I_a}{10^{15}\mathrm{Wcm}^{-2}}\right)^{5/9} \left(\frac{t}{100\mathrm{fs}}\right)^{7/9} \mathrm{nm} \tag{8}$$

and the surface temperature

$$T_e(0) = 119 \left(\frac{n_e}{10^{23}\text{cm}^{-3}} \right)^{1/12} Z^{1/12} \left(\frac{I_a}{10^{15}\text{Wcm}^{-2}} \right)^{1/3} \left(\frac{t}{100\text{fs}} \right)^{1/6} \text{eV}. \tag{9}$$

2.2.2 Ablation

Ablation denotes the removal of matter from a target upon laser impact. This can be used in medical applications such as dermatology (tattoo removal), but also causes troublesome effects e.g. in optical components of laser facilities [15]. The emission of heavier target constituents occurs due to energy input into the target, i.e. heating, causing it to overcome the solid binding energy. The core motion, increase of kinetic energy and thus emission of atoms, is, as discussed above, a secondary motion based on the electron motion. The electrons are getting excited across the band-gap of the material by multiphoton absorption. A Ti:Sapphire laser for example emits 1.55 eV photons, so the number of photons necessary for overcoming the band-gap is

$$n = \text{int}\{E_{\text{gap}}/1.55\text{eV}\} + 1. \tag{10}$$

Electrons near the surface, with depth smaller their mean free path, then leave the target and the heavier ions follow, due to the resulting charge gradients.

The electron motion occurs instantaneously during the short laser pulse, leaving behind positively charged areas at the target surface. Bulk electrons then fill these regimes again, but if they are too slow and the fleeing electrons are too fast, the regions are positively charged for a considerable time and become unstable. This can lead to a so called Coulomb explosion, meaning the surface breaking apart and emitting positively charged particles due to the subsequent electrostatic repulsion of the atoms in the homogeneous charged area. This is a non-thermal effect.

An important aspect in portraying ablation is the use of short pulses ($<$100 fs), because else secondary effects, like the laser interacting with ablated material, may become relevant. In the short pulse study the absorption properties are also not affected, so the laser interacts with an almost passive target and all significant modifications occur after the pulse.

A parameter to predict the ablation velocity is the ion sound velocity c_{si}, which describes the speed of an ion density modulation in the target, driven by a pressure wave [16]. As long as there are no other UHI dynamics happening at the same time, e.g. compression, making the sound velocity a function of density, it is a reasonable marker for the ablation velocity [6]. Based on the ideal gas equation of state, the sound velocity is

$$c_{si} = \sqrt{\frac{\gamma_e Z k_B T_e + \gamma_i k_B T_i}{M}}, \tag{11}$$

with k_B the Boltzmann constant, Z the charge, T_e/T_i the temperature and M the ion mass. Corresponding to the electrons moving so fast relative to c_{si}, that they have no time to equilibrate their temperature everywhere, γ_e is set to 1. The ion factor γ_i on the other hand is set to 3, because ions experience a 1D compression in a plane wave [16].

2.2.3 Hole Boring

For finite spot sizes (2-10 μm) or extreme irradiances ($I\lambda^2 > 10^{18}$ W) the light can cause a hole of several wavelengths through the moderately overdense plasma. This is caused by a pressure imbalance for high intesities:

$$\frac{P_L}{P_e} = \frac{2I_0/c}{n_e k_B T_e} \simeq \frac{660 I_{18}}{160 n_{23} T_{keV}} \gg 1 \tag{12}$$

with P_L the light pressure and P_e the plasma pressure. I_{18} is the laser intensity in units of 10^{18} Wcm^{-2}. The electron density n_{23} is in units of 10^{23} cm^{-3} and electron Temperature T_{keV} in keV. This imbalance pushes the plasma inwards, preferentially at the center of the focal spot size, which causes an electrostatic bow-shock to form. This density continuity travels into the target with a constant velocity. Solving the 1D continuity and momentum conversation equations [23] the hole boring velocity becomes [17]:

$$\beta_b = \frac{v_b}{c} = \left(\frac{(2 - \eta_a) I_0 \cos\theta}{2\rho c} \right)^{1/2} = \left(\frac{Z m}{M} \frac{n_c}{n_e} \frac{(2 - \eta_a)\cos\theta}{4} \frac{I_{18}\lambda_{\mu^2}}{1.37} \right)^{1/2} \tag{13}$$

Considering a relativistic hole boring regime ($\Xi = I/\rho c^3 > 1$) the veloctiy corrrects to

$$\beta_b = \frac{v_b}{c} = \frac{\sqrt{\Xi}}{1 + \sqrt{\Xi}} \tag{14}$$

with the dimensionless pistoning parameter Ξ, as in [18].

2.2.4 Ion Acceleration

Depending on density and laser intensity plenty acceleration mechanisms can occur, such as target normal sheath acceleration (TNSA), collisionless shock wave acceleration (CSA) or radiation pressure acceleration(RPA). In an electron density regime of $n_e \sim 10^{23}$ cm^{-3} and for laser intensity $I_L \sim 10^{17}$-10^{22} Wcm^{-2}, the dominant process is TNSA, while RPA can occure for the upper intensities.

Target normal sheath acceleration is driven by a fraction of the electrons that energizes to much higher energies than the bulk electrons, which are energized by collisional heating. Collisionless absorption, such as resonance absorption, causes this super heating. Even though the electrons

are accelerated by a coherent electric field, the random nature of the electron acceleration in standing wave fields causes strong cycle-to-cycle fluctuations in trajectories and energies acquired [13]. Therefore the single-temperature electron distribution turns into an electron distribution with two scale lengths T_e (bulk electrons) and T_h (highly energized electrons). For high laser intensities ballistic electrons (collisionless) travel through the target and escape several Debye lengths into vacuum on the rear side. Because of the charge separation a sheath field E_s arises, normal to the surface and spreading several Debye into vacuum. The field is strong enough to accelerate the ions at the rear surface, preferably light ions or contaminant protons. Their energy depends onto the field strength, which depends on the parameters of the electrons (average energy, number, divergence) as well as the density profile of the rear surface [14].

Radiation pressure acceleration for thick targets happens due to the hole boring mechanism. The plasma surface is pushed inwards and ions are reflected on the deformation front, which accelerates them towards the rear. For thin targets, $d \ll v_{HB}\tau_L$, RPA happens in "light sail" mode, where the entire target gets accelerated. A thick target, as the ones in this work, should also satisfy $a_0 < \pi \frac{n_e}{n_c} \frac{d}{\lambda_L}$ to ascertain that it does not get transparent in the HB process. Here a_0 is the dimensionless laser intensity, d is the target thickness and n_e is the electron density. The setup of a Ta:Si laser ($\lambda = 800$ nm) with maximum Intensity I $= 10^{22}$ Wcm^{-2} and a target with electron density $> 800\ n_c$of width $d = 1000$ nm meets this claim.

3 Computational Method

3.1 Particle-in-Cell (PIC) and SMILEI

Solving the complex task to simulate a plasma is usually done in one of two models. The first is a fluid description based on the Navier-Stokes equations [20], the second is a kinetic description considering more detailed models of the dynamics. The particle-in-cell (PIC) algorithm is a kinetic approach and based on the Vlasov-Maxwell system of equations for collisionless plasma. For the PIC method the respective distribution functions $f_s(t, x, \mathbf{p})$ of the particle species, each species s characterized by their charge q_s and mass m_s, satisfy Vlasov's equation:

$$(\partial_t + \frac{\mathbf{p}}{m_s\gamma} + \mathbf{F}_L \cdot \nabla_{\mathbf{p}})f_s = 0, \tag{1}$$

with $\mathbf{F}_L = q_s(\mathbf{E} + \mathbf{v} \times \mathbf{B})$ being the Lorentz-Force acting on a particle with velocity $\mathbf{v} = \frac{\mathbf{p}}{m_s\gamma}$, the relativistic Lorentz factor $\gamma_s = \sqrt{1 + (\mathbf{p}/m_s c)^2}$ and the speed of light c. The large amount of particles is modeled by fewer so called macro-particles which discretizes the distribution $f_s(t, x, \mathbf{p})$ to a sum of N_s of these quasi-particles. Due to the Lorentz force only depending onto the charge-to-mass ratio, they follow the same trajectories as the up to millions particles they contain.

The electric $\mathbf{E}(t, \mathbf{x})$ and magnetic $\mathbf{B}(t, \mathbf{x})$ fields are interpolated on a staggered grid, the Yee-grid, dividing the simulation volume. They satisfy Maxwell's equations:

$$\begin{aligned}
\nabla \cdot \mathbf{B} &= 0 \\
\nabla \cdot \mathbf{E} &= \rho/\epsilon_0 \\
\nabla \times \mathbf{B} &= \mu_0\mathbf{J} + \mu_0\epsilon_0\partial_t\mathbf{E} \\
\nabla \times \mathbf{E} &= -\partial_t\mathbf{B}
\end{aligned} \tag{2}$$

with μ_0 and ϵ_0 being the vacuum permeability and permittivity. The fields determine the macro-particle motion, which in turn creates currents and leads to new fields which again drive the particles. This process is called the PIC-loop:

0. Initialization: loading particles, computing initial charge/current onto the grid and initial fields,

1. Field interpolation at the particle position,

2. Particle pusher: computing the new particle velocities and positions,

3. Projecting charge and current onto the grid,

4. Maxwell solver: computing the new fields onto the grid.

The PIC-code used for the simulations in this work is SMILEI, a collaborative, open-source, object-oriented (C++) code [22]. It was run on CPU-nodes of the HPC facility 'Hemera' at Helmholtz-Zentrum Dresden Rossendorf (HZDR).

3.2 Accuracy Conditions

To ensure, that the simulation represents reality, several accuracy and stability conditions have to be fulfilled. They are either connected to the physics of the problem or the numerical method. An important example for the latter is the Courant-Friedrich-Lewy-condition [21] which determines the relation between cell-length $\Delta\mu$ ($\mu = (x, y, z)$) in the grid and the duration of one time-step Δt:

$$\Delta t_{CFL} < \sum_{\mu} (\Delta\mu^2)^{0.5}. \tag{3}$$

Furthermore the values for macro-particles per cell, boundary-conditions, box size, etc. have to correspond to the geometrical setup, as well as the scale of the physics that are portrayed. Not all relevant parameters can be listed here and not all can be assigned to exact formulas as above, but important to stress is, that simulations have to be set reasonable in order to become a powerful tool.

3.3 Simulation Setup

The simulations consist of a 2D box, 10 μm in x direction and 0.15 μm in y direction, a target at x = 5 μm, as seen in Figure (3.1) a), and a λ = 0.8 nm laser pulse entering from the left side (x-longitudinal, y-transverse) with pulse duration τ = 40 fs (FWHM) and incidence angle α = 17°. The physical 1D setups were simulated in a 2D box, a small transverse width paired with periodic boundary conditions allowing the layers to intertwine when heated, yet still display a 1D geometry. Periodic boundary conditions bring particles and fields at the boundary back inside the box, which distorts the energy evolution in 2D, since no particle or energy is lost in transverse direction, but agrees with a 1D setup.
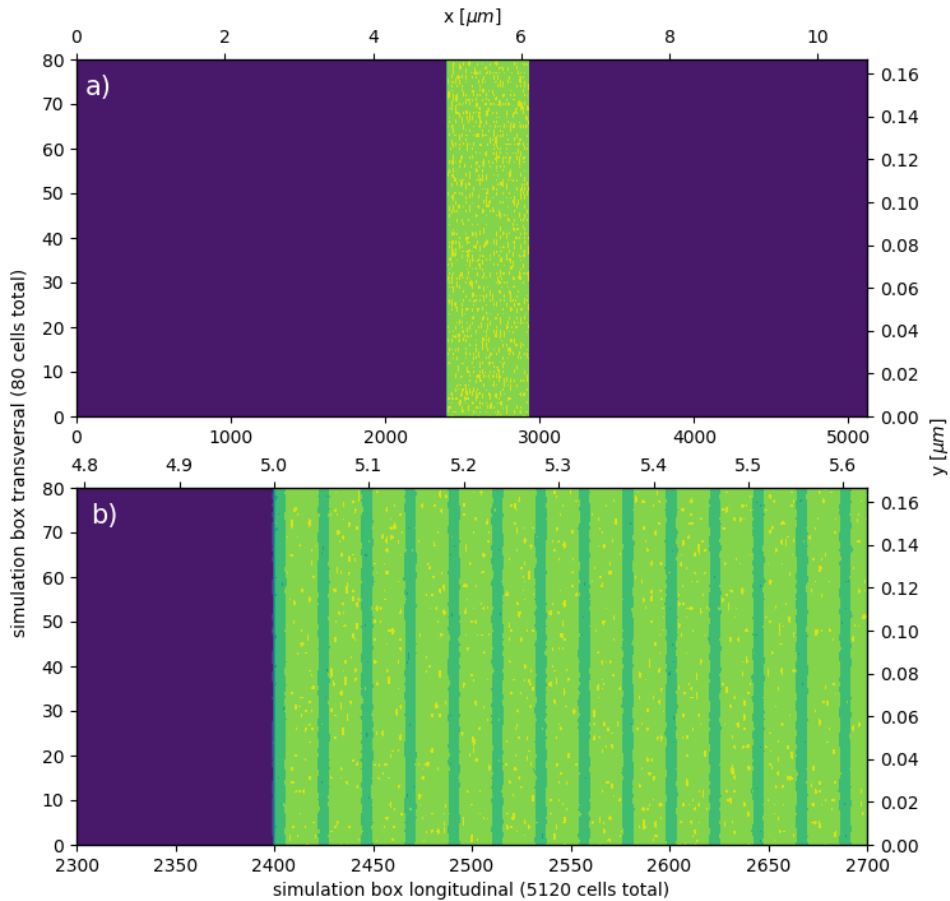
Figure 3.1: Simulation box at time 0 fs for n = 24 ML.

The target contains multi layer, i.e. two materials in repeating layers of predefined thickness and amount, as in Figure (3.1) b). In an experiment the ML are on top of a silicon support and behind an aluminum shield (Shield,ML,Support). The support is where the ML are put on in the target making process, the shield prevents a too-fast heating due to direct laser impact or a destruction, e.g. by hole boring. Even though we try to simulate according to an experimental

setup, it turned out to be reasonable for this work to implement a target fully containing ML, total target thickness $d_{total} \simeq 1\ \mu m$, with neither support nor shield. It was not clear how thick a shield should have been in order to stop the heavy laser impact yet still hinder the ML to be utterly impassive. Therefore one has to get rid of the shield and take into account that a couple of ML are for sure getting destroyed, so should increase the total amount of layer at the front. Additionally, ion acceleration at the back of the target becomes more relevant for the UHI regime. That raises the interest of applying GISAXS not only at the front but also the back side of the target, hence needing ML behind the support as well. That would raise the same question of thickness of the support as for the shield. After all it was the most efficient to implement a pure ML target to be sure not to miss something and then predict how thick a shield and a support should be. It later turned out, that we can even reason to not use a shield or support in the experiment as well, because that allows to observe the density oscillation dynamics. Table 3.1 shows the most relevant parameter of the input setups. We will mainly

nb.	I [Wcm^{-2}]	d_1 [nm]	d_2 [nm]	d_{total} [nm]	n layer	$resx$	PPC
1	$10^{17} - 10^{22}$	Ta - 12.55	Cu$_3$N - 33.33	1100	24	384	36
2	10^{20}	Ta - 12.55	Si - 33.33	1100	24	384	36
3a	10^{20}	Ta - 6.3	Si - 16.8	1100	24	384	36
3b	10^{20}	Ta - 12.55	Si - 33.6	1100	24	192	36
3c	10^{20}	Ta - 25.2	Si - 67.2	1100	24	192	36

Tabelle 3.1: Input parameter of the simulations.

use the 6 simulations of setup no.1 for the evaluation. The other 4 setups will be analyzed regarding the parameter scan of the density oscillation. Number of layer n denotes the amount of layer for each material. The materials of the layers in setup no. 1 are tantalum and copper nitrite, which were chosen based on the reference set up [6]. Tantalum and silicon were chosen for the second setup to steepen the electron density gradient between the layers. The density of copper nitrite in setup 3 is modified to a quarter of its solid density for the same reason, as will be further discussed later on.

4 Results

4.1 Setup Test

As mentioned in 3.3, the setups were simulated in a semi 2D geometry, which means a very thin 2D simulation box, instead of a 1D geometry, which requires less computational workload. The reason for that is, the restriction of intermixing of the ML is restricted in 1D, compared to 2D. This results in the ML structure artificially "surviving" longer in 1D. Remember that the ML structure is defined by the density difference in between the layers, which decreases when the layers intermix. The layers are only visible in the GISAXS pattern, when there is a significant, $t_{GISAXS} = 200$ n$_c$, decrease of density in between the layers. A 1D geometry that allows the layers to stand longer than in a real setup therefore misrepresents whether we would see certain effects in the GISAXS pattern. To avoid that it was chosen to simulate in semi 2D. Of course a real 2D or 3D setup would represent the densities even better, but the computational workload grows a lot with higher dimension.

Mixing occurs when the ions of the layers diffuse into each other due to collisional diffusion or instabilities, e.g. the Rayleigh-Taylor instability (RTI). While the former occurs in both geometries, slower in 1D than 2D, the latter can only form in the 2D setup.
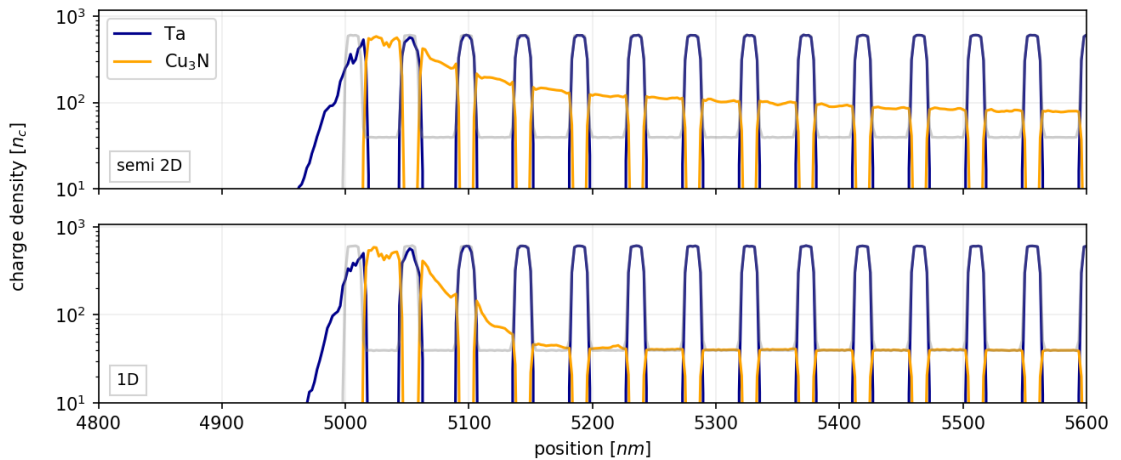
Figure 4.1: Ion density profile for 1D and semi 2D setup, I $= 10^{17}$ Wcm^{-2} and t $= 150$ fs.

Lets take a first look at the diffusion in both dimensions. Figure (4.1) shows the comparison of a semi 2D and 1D geometry at t =150fs, t in general always relative to when the laser pulse maximum hits the target surface. The comparison shows that in 1D only the first 3 copper nitrite layers ionize while in 2D all visible layers increase in charge density, so lose electrons due to collisional ionization. The ionization occurs slower in 1D compared to semi 2D, because the diffusion dynamics are restricted. Energized electrons moving through the target and losing energy due to collisions, causing ionization and heating the target, happens slower when all electrons move in one dimension, because the collision cross section reduces to 1D. Slower heating causes slower intermixing, because the ions first have to overcome their solid structure and gain thermal energy in order to diffuse into each other. Additionally, even when heated, the ions can only move in one dimension, just like the energized electrons, which also restricts the mixing.

The second cause of mixing are instabilities on the surfaces between the layers. Here we want to look into the Rayleigh-Taylor-instability. Hydrodynamic RTI appears on an interface of two fluids of different densities, the lighter one pushing the heavier fluid [24]. A simple example represents water above oil, the first pushing into the second due to the gravitational force. In a plasma curved magnetic fields cause the "gravitational" force. Small ripples on the interface between the layer, generated by random thermal fluctuations, grow and cause a density perturbation [16], leading to intermixing. Naturally, this appears only in a 2D or 3D geometry, where a surface between the layers can be defined. This adds to the faster diffusional mixing in 2D. Figure (4.2) shows surface ripples occurring in the semi 2D simulations, which can be connected to the RTI, as in [25].
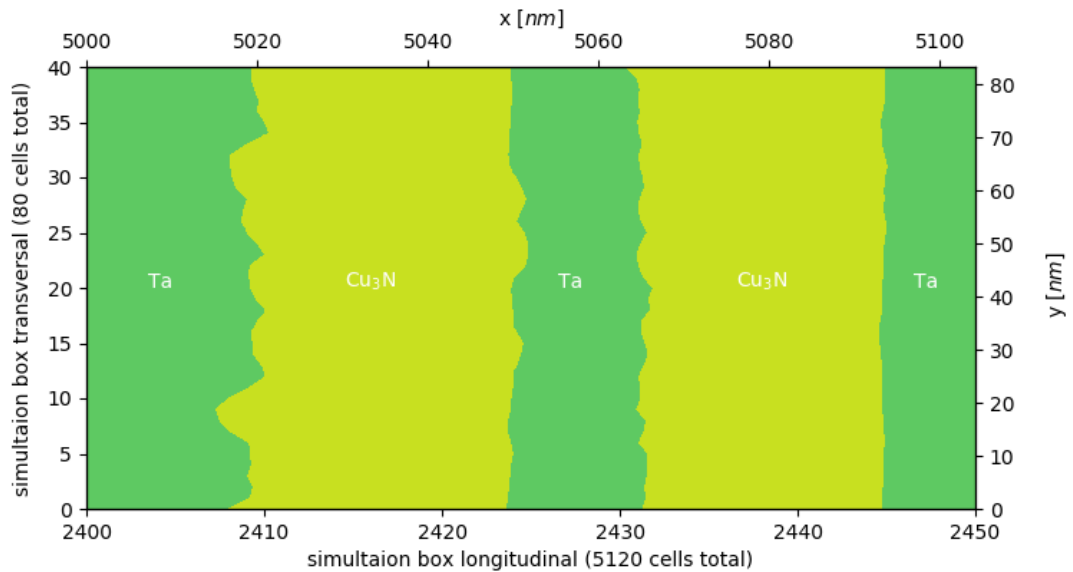
Figure 4.2: Layer surface ripples for I $= 10^{17}$ Wcm^{-2} at t $= 800$ fs for simulation setup nb.1.

A final reason to switch to a 2D setup is that a density profile as in Figure(4.1), with an exponential tail, can only be resolved in a 1D simulation when the number of macro-particle per cell is set high enough. The 1D setup above for example required 2280 particles per cell in order to match the 2D setup with only 36 particles per cell and 80 cells in transverse direction, so the number of particles per one cell in x direction would be equal. Therefore a 1D simulation barely offers reduction in the computational work required. Finally, it was most efficient to implement semi 2D simulations in the existing simulation framework.

4.2 General Dynamics

In this section we will take a brief and general look at the target. The goal is to judge what we can see in a GISAXS pattern and what we will not be able to see. At this point we will use the density resolution d_{GISAXS} and time resolution t_{GISAXS} to estimate the feasibility. Remember at this point, that the GISAXS pattern requires an intact ML structure, meaning a difference in electron densities between the layers of significant amount in order to display the profile.

4.2.1 Target Front

Even though one of the most interesting regimes of laser target interaction is particle acceleration, mostly happening at the rear side of the target, the front side of the target also represents an interesting regime to investigate. For example the absorption of laser energy, the creation of energized electrons and ablation are areas of great interest.
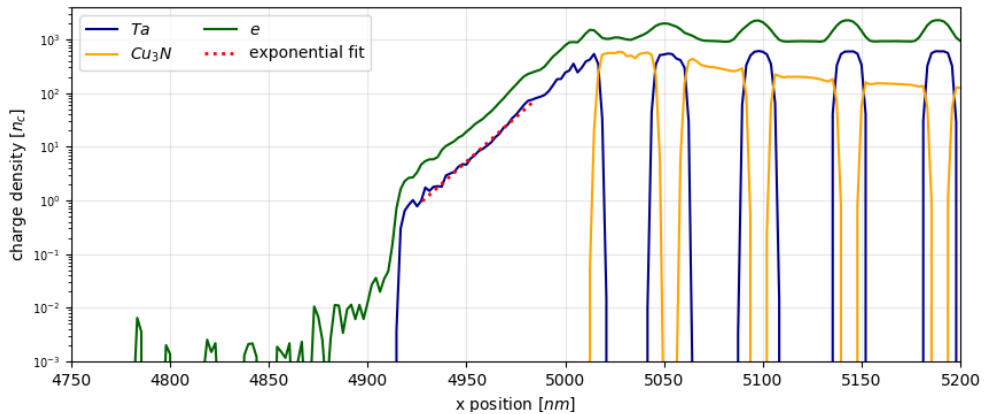
Figure 4.3: Ion and electron density profile for I $= 10^{17}$ Wcm^{-2} at t $= 250$ fs.

We will first take a closer look at ablation, i.e. the ion expansion into vacuum. The removal of target constituents was discussed in the reference paper as well and it is therefore appropriate to extend these studies. It is displayed in Figure(4.3) for an Intensity I $= 10^{17}$Wcm^{-2} and simulation setup no. 1 at t $= 250$fs. For the green electron profile bound and free electrons are considered. The electron density tail is expanded further than the blue ion tail, former pulling the latter due to electrostatic forces. This is caused by the laser energy mainly interacting with the lighter electrons, allowing them to gain energy and leave the target first, as discussed in 2.2.2..

In the simulation the scale length L_s of the exponential tail was chosen to be the marker for the ablation. Therefore the exponential tail was fitted, as seen in Figure (4.3) to determine $L_s(t)$ and therefore the ablation velocity.

Figure (4.4) shows $L_s(t)$ for the 4 intensities, I $= 10^{17}$-10^{20} Wcm^{-2}. Both higher intensities cause the target to get majorly compressed, even destroyed after 200 fs for I $= 10^{20}$ Wcm^{-2}, as

seen in figure(4.7) and (4.8). Therefore they were not considered for the scale length. One can observe that the plasma expansion is faster for higher intensities. This is caused by the electron energy T_e scaling with the laser intensity. Higher values of T_e lead to a faster expansion of the electrons and therefore a faster expansion of the ions.
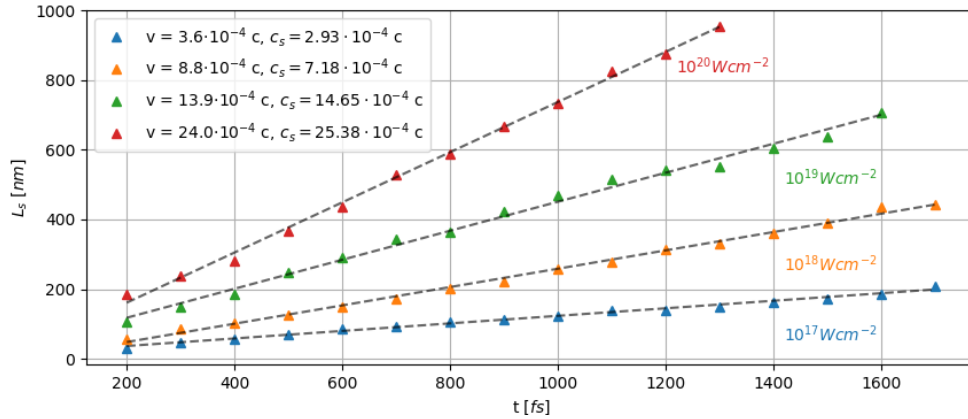
Figure 4.4: Scale length L_s for $I = 10^{20}$-10^{17} Wcm^{-2} at target front.

We can compare this to the scale length of [26], which predicts $L_s = c_s t$. Both the measured scale length in figure (4.4) and the model depend linear on time. The comparison of ablation velocity v and ion sound velocity c_{si} also shows fair agreement. The sound velocity c_{si} was calculated with the electron temperature T_e at the front bulk of the target (t = 25 fs) and formula (11) for the tantalum ions. We see, that measuring the scale length in an experiment would allow us to determine the ablation dynamic, but also the ion sound velocity $c_{si}(T_e)$ and therefore the electron temperature T_e with formula (11).
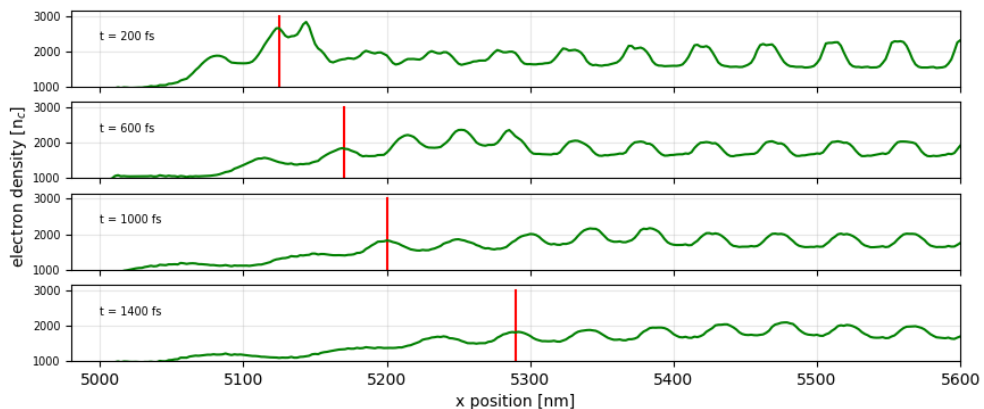
Figure 4.5: Electron density for 10^{20} Wcm^{-2} and position of first layer with height > 200 n_c (red)

The scale length L_s is a good example of a highly interesting value, that GISAXS is not able to portray. Figure (4.5) shows the total electron profile for $I = 10^{20}$ Wcm^{-2}. GISAXS is sensitive

only for peaks and therefore over looks the exponential tail at the target front. The red line denotes the first peak, that is recognizable in the scattering pattern after the density sensitivity as defined in 2.1 ($n_{GISAXS} = 200$ n_c).

Another way of measuring the ablation is to count how many layer peaks have been destroyed, i.e. fall under 200 n_c, in a certain time. Also, one could measure the movement of the first recognizable layer peak, i.e. the first peak that has a height of at least 200 n_c as in figure (4.5), in the target. This has been done in the reference setup [6]. Both methods mark the ion expansion and therefore allow to determine a velocity that characterizes the ablation. They are also GISAXS compatible, because they consider $n_{GISAXS} = 200$ n_c, when defined as above.
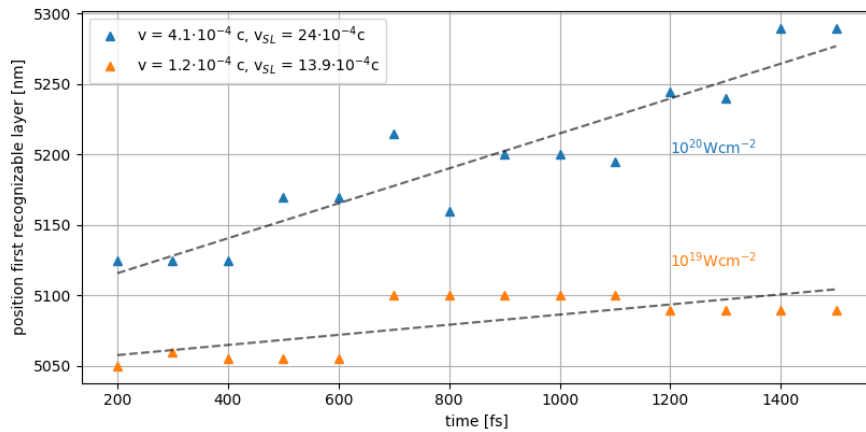
Figure 4.6: Position first layer with electron density peak $> 200n_c$ for 10^{19}-10^{20}Wcm^{-2}.

Figure (4.6) shows the positions of the first recognizable layers for I $= 10^{20}$ Wcm^{-2} and the corresponding ablation velocity. For the lower intensities it was not possible to determine a velocity because the first layer did not move within 2ps. The plot shows, that the front layer is not consistently moving linear in time. For some times, the layer does not move at all and for others there is a jump to a next position. This happens because the front layer heats and expands, which causes the density peak to widen and finally dissolve into the exponential tail. When the peak height falls under 200 n_c, the next peak in the target becomes the first recognizable layer, which causes the jump in the plot.

The extracted ablation velocity v is smaller than the scale length velocity in figure(4.4). We can also see, that the quotient of the velocities $v_{20}/v_{19} = 3.4$ for the two intensities is not consistent with the quotient of the scale length velocities $v_{20}^{sl}/v_{19}^{sl} = 1.7$ of figure(4.4). Therefore for this special case it is not possible to measure the ablation velocity with the position of the front. It would probably be more reasonable to follow the first peak for longer times to minimize the impact of the jumps. This is however not always possible in the high intensity regime, because the layers heat faster than for lower intensities. The heating causes also the

bulk layers to expand and intermix, which causes the peak structure to smooth out. Therefore we can predict, that the target will not be recognizable in a GISAXS pattern. The velocity of the front peak as in figure(4.5) is also influenced by multiple front dynamics, like ablation and compression, that influence the electron density profile. This causes the velocity to not be an ablation marker anymore. For lower intensities there is no compression and the ablation velocity can be defined, as in [6].

When the target experiences a major compression, the movement of the first recognizable peak is barely influenced by the abation anymore. Figure (4.7) shows the compression of the target for I $= 10^{21}$ Wcm^{-2}. Following the first recognizable peak with a GISAXS diagnostic here would therefore mark the compression velocity. Here it is not relevant when the first peak jumps as described above, because the total front movement is relatively large. Finally we
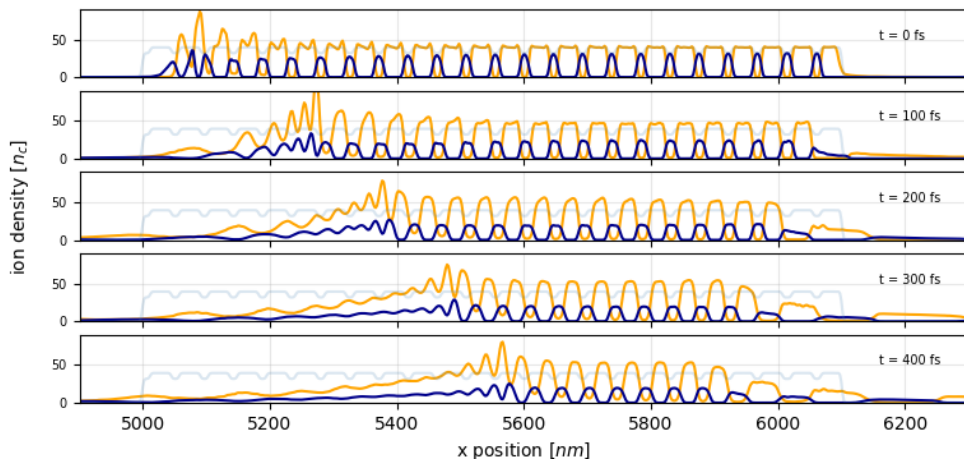
Figure 4.7: Ion density (tantalum - blue, copper nitrite - orange) for 10^{21} Wcm^{-2} for simulation setup no.1.
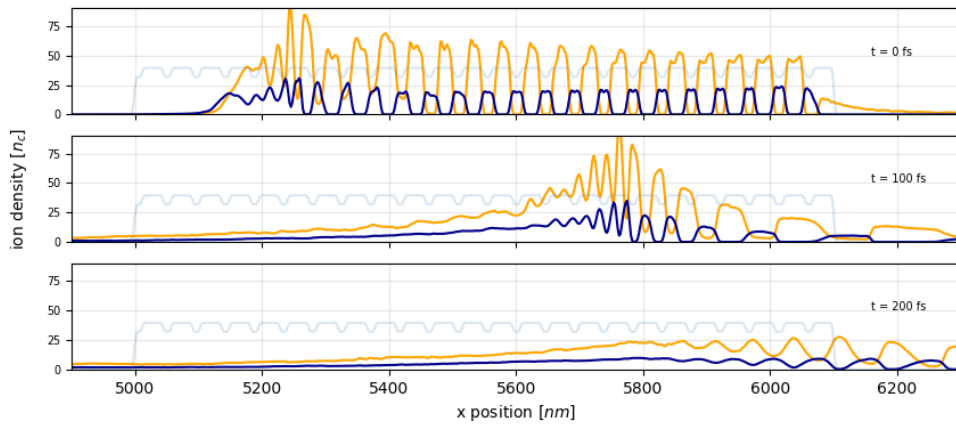
Figure 4.8: Ion density (tantalum - blue, copper nitrite - orange) for 10^{22} Wcm^{-2} for simulation setup no.1.

can conclude, that the density resolution $n_{GISAXS} = 200$ n$_c$ allows to portray the compression

velocity for the higher intensities, but not an ablation velocity.

When now looking at the time resolution $t_{GISAXS} = 500$ fs and at figure(4.7), we realize that one would need a higher resolution in order to capture the compression. The time resolution can be raised by using mass-limited targets [27]. With figure(4.7) we can recommend to seek for a time resolution of at least 100 fs.

4.2.2 Target Rear

In agreement to the last section, we will now take a look at the target rear side. This region is interesting because of the particle acceleration mechanisms. For the setup and applied laser intensities one expects target normal sheath acceleration (TNSA). The ions are accelerated normal to the rear surface, by electrons leaving the target and creating a high electric field. These ballistic electrons gain high energy from the laser pulse, cross the target instantaneously and expand into vacuum at the rear.
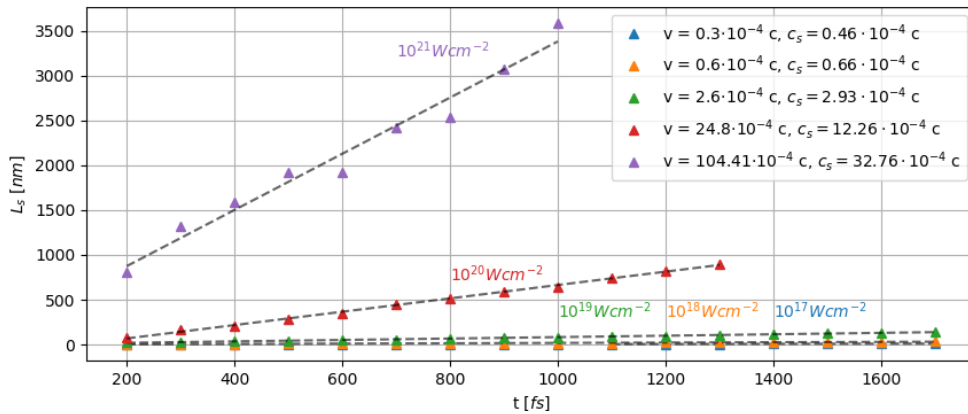
Figure 4.9: Scale length L_s for $I = 10^{20}$-10^{17} Wcm^{-2} at target rear.

Figure (4.9) shows $L_s(t)$ for 5 intensities, $I = 10^{17}$-10^{21}Wcm^{-2}. Here we were able to include 5 intensities, only neglecting the highest, because of the destruction, as seen in figure(4.8). In figure (4.9) we can again see agreement with $L_s = c_s t$ [26] in terms of linear time dependency. For the lower 3 intensities $I = 10^{17}$-10^{19}Wcm^{-2} (blue, orange and green) the velocities also fairly agree again. For the upper two velocities however, the expansion happens much faster than predicted with the ion sound velocity c_s. The model of [26] predicts the ion expansion based on the bulk heating and does not consider relativistic effects. In the non relativistic regime mainly the thermal bulk electrons cause the expansion. For relativistic intensities however, there are the ballistic electrons, that leave the target rear and cause ion acceleration, as mentioned above and in section 2.2.4. The high sheath field causes ion acceleration, i.e. fast ion expansion. The backside expansion is therefore faster for higher intensities, because relativistic expansion is greater than the thermal expansion. This causes the velocity of the simulation scale length v_{SL} to be much higher than predicted by the thermal model [26].

Without further analyzing the electron density profiles, we can estimate the GISAXS feasibility. There will not occur compression, that impacts the electron density profile, at the target rear side. It is therefore reasonable to count the position of the first recognizable layer in order to measure the expansion. Also, one should again use mass-limited targets [27] to increase the time resolution.

4.3 Density Oscillation

Now we want to take a closer look at the density oscillation dynamics to see what kind of physics GISAXS would allow to observe. There was no evidence of literature that already describes this dynamic. Nevertheless, it is a simple mechanism, one could easily recreate in an experimental setup.

4.3.1 Basics

In this first section we want to understand what dynamics we call density oscillation and how it portrays. The next sections will then offer a physical description and parameter scan.
When looking at the density profile of the ML over time, one can observe a density oscillation. Before getting into the detailed description of what is happening it is worth looking at the whole target, to see how the dynamics are visible. Figure (4.10) shows the total ion (black) and electron (green) charge density profile over time for simulation setup no.1 at I = 10^{20}Wcm^{-2}. Remember at this point that the ML structure is defined by the different densities between the layers, the peaks in the profiles in figure (4.10).
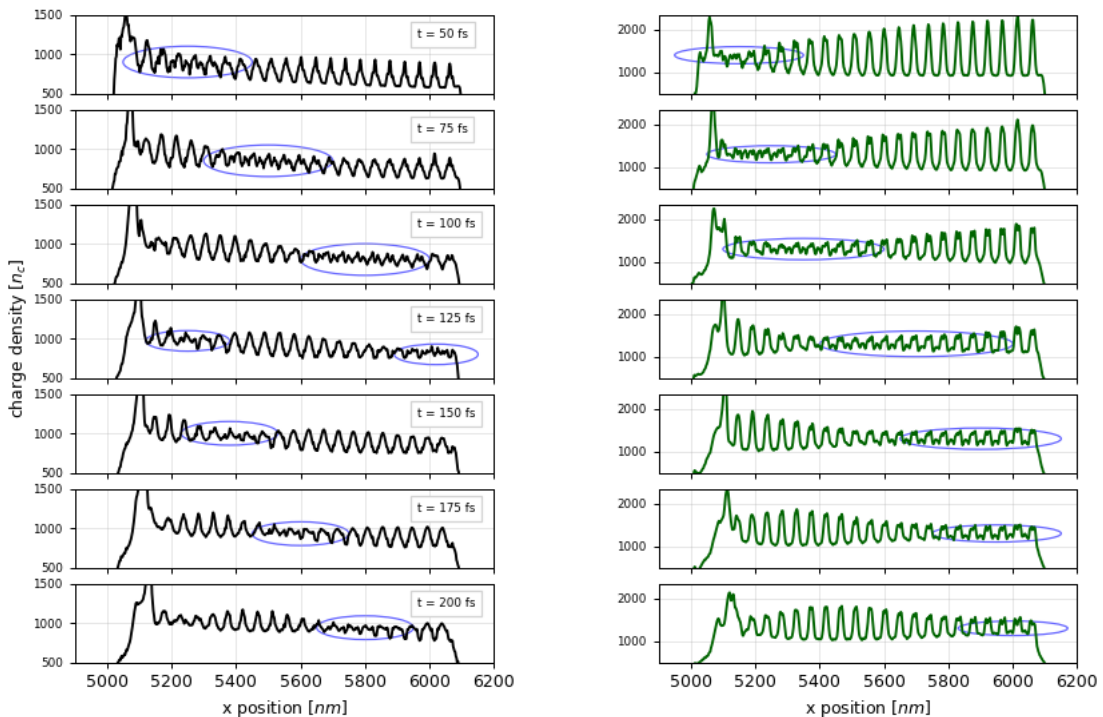
Figure 4.10: Ion (black) and electron (green) charge density over time for I = 10^{20} Wcm^{-2} and setup no. 1.

When now looking at the blue circled areas, one can see that the ML structure is destroyed there, no or barely regular peaks are apparent for both ions and electrons. Lets call this area a density alteration because it varies from the original ML profile. For the case of Figure (4.10) the ion density alteration appears at the front of the target at t = 50 fs, reaches the end of it at t = 125 fs, while a new one forms at the front again. The reappearance of the density alteration leads to the idea of identifying it as a density alteration wave, but later on it will become apparent why it is not a wave and why this name could be misleading by comparing it for example to a plasma wave.

Because this is happening on a subpicosecond timescale, one can conclude that the alteration is not caused by heating. Even though heating of the ions would cause them to lose their ML structure and form one plasma bulk, because of diffusive intermixing, this is not expected in less than a picosecond, as mentioned in 2.2.1. Additionally heated ions are not able to recover and find their ML structure again, which is happening to the peaks in figure (4.10) after the alteration passes. Therefore the density alteration traveling through the target is not directly caused by a heat wave.

Now comparing the electron and ion profile, one can see that for both the density alteration is excited at time t = 50 fs at the front of the target. For the times t = 50 fs-125 fs the electron density alteration however follows the ion density alteration behind. A second electron alteration does not appear, even though it does for the ions. The detailed layer profiles will later reveal why this is happening and what dynamic we see in each profile. At this point it may seem vague to interpret the total electron and ion profiles instead of the single layers, as we will soon, but one has to remember that an experimental setup does not allow to portray the single layer densities. For example the GISAXS approach only allows to determine the total profile of the electrons, as mentioned in 2.1.. It is therefore useful to see the dynamic as one would see it in the results of an experiment to ensure that this effect may become relevant.

A final observation from figure (4.10) is the decrease in velocity between the first (<125 fs) and second (>125 fs) ion density alteration. While the first one needs 75 fs (50 fs - 125 fs) to cross the target, the second one needs a little more, only almost reaching the end of the target after 75 fs (125 fs - 200 fs). This leads to the assumption that a damping mechanism occurs, which should be subject to further research.

Lets focus on the single layers to understand what actually oscillates. Figure (4.11) shows the same setup as above for t = 75 fs. The ion profiles at the bottom of figure (4.11) reveal three different regions. The first from the front, where the copper nitrite charge density (orange) exceeds (5120-5320 nm), the second, where the layer densities are fairly equal (5400-5700 nm) and the third region at the back, where the charge density of tantalum (blue) exceeds slightly (5700-6100 nm). One can also identify the regions in the profile of the free electrons (green), which is identical to the charge density in figure (4.10), because the inner target stays semi

neutral after the laser interaction. The first and third region show the ML structure, while the second region shows the density alteration as discussed above.
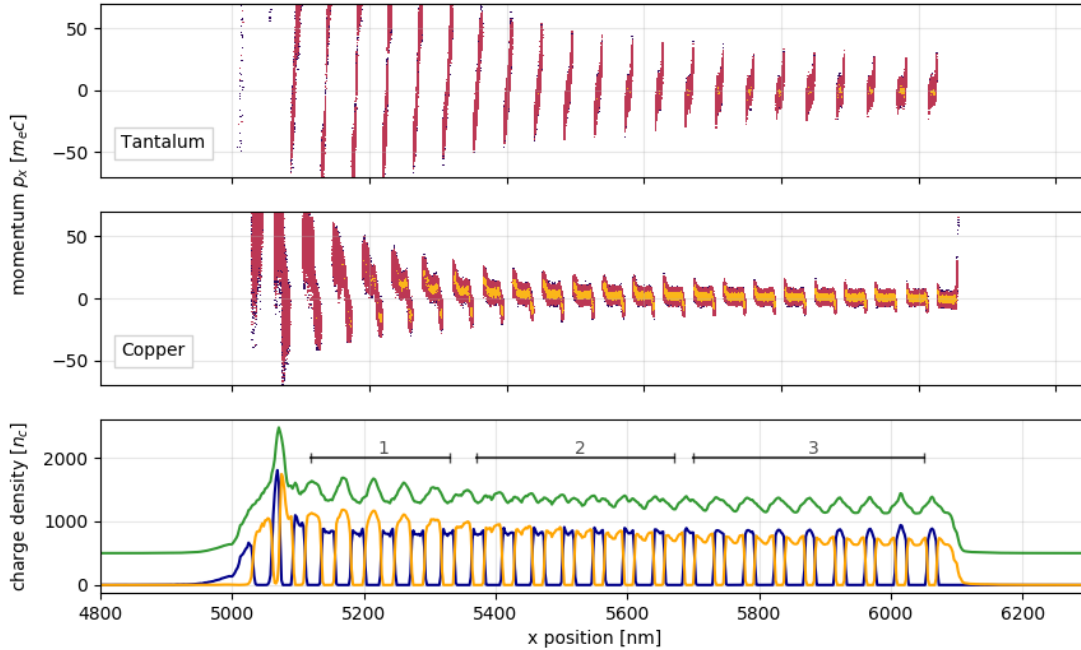
Figure 4.11: Density profile and phase space of ion species and free electrons (green) at t = 75 fs for I = 10^{20} Wcm^{-2} and setup nb.1.

The phase spaces of the third region show that the tantalum layers expand, while the copper nitrite layers are being compressed, hence a double peak structure. The expansion or compression can be detected by looking at the front and back of the single layers in the phase spaces. When the tail in the front of a layer has positive momentum it moves inside the layer, showing compression. For an expansion on the other hand the front tail has negative momentum, meaning the particles move away from the layer. It behaves in reverse for the tail on the back side of a layer.

The expansion of tantalum and compression of copper nitrite stagnate when looking further at the front of the target, tantalum layers developing a double peak structure as well. When looking at later times and higher energies this becomes a more obvious inversion of the phase space. Figure (4.12) displays the setup for I = 10^{21}Wcm^{-2} at t = 125fs, compression of tantalum and expansion of copper nitrite apparent.

It is important to realize at this point that these three regions, even though showing one time step, allow us to analyze the dynamic over time. Third region happening first, then second and first, because they move through the target, starting at the front.

We can conclude that the one layer with higher ion charge density, lets call it the dominant layer, expands and compresses the other layer, the recessive one. In the third region in figure

(4.11) tantalum is the dominant layer and copper nitrite the recessive. The compression leads to a rise in density of the recessive layer, causing the densities to become fairly equal and destroy the ML structure because one can not distinguish between the layers anymore, as in the second region in figure (4.11). This is what we called a density alteration. The compression of the recessive layer finally causes it to gain a higher charge density than the dominant layer, making it the new dominant layer. This happens in the first region of figure (4.11), where copper nitrite now is the layer with higher charge density.

This finally portrays that the layers alternate in expanding, i.e. decreasing in charge density, and getting compressed, i.e. increasing in charge density. The oscillating value therefore is the charge density of the single layers. Later on we will be discussing the differences and similarities of charge and number density. We will also soon understand what causes the dynamics.
The ion density alteration in Figure(4.10) follows the density alteration, the region where the layers switch in roles. It therefore allows us to follow the dynamic over time.
The electron density in Figure(4.10) follows the movement of the tantalum ions because their electrons dominate the electron profile. The ML structure is expressed in the electron profile when tantalum is the dominant layer and is almost smoothed out when it is not. Even when being the recessive layer, tantalum still has only slightly lesser electrons than the dominant copper nitrite layers.
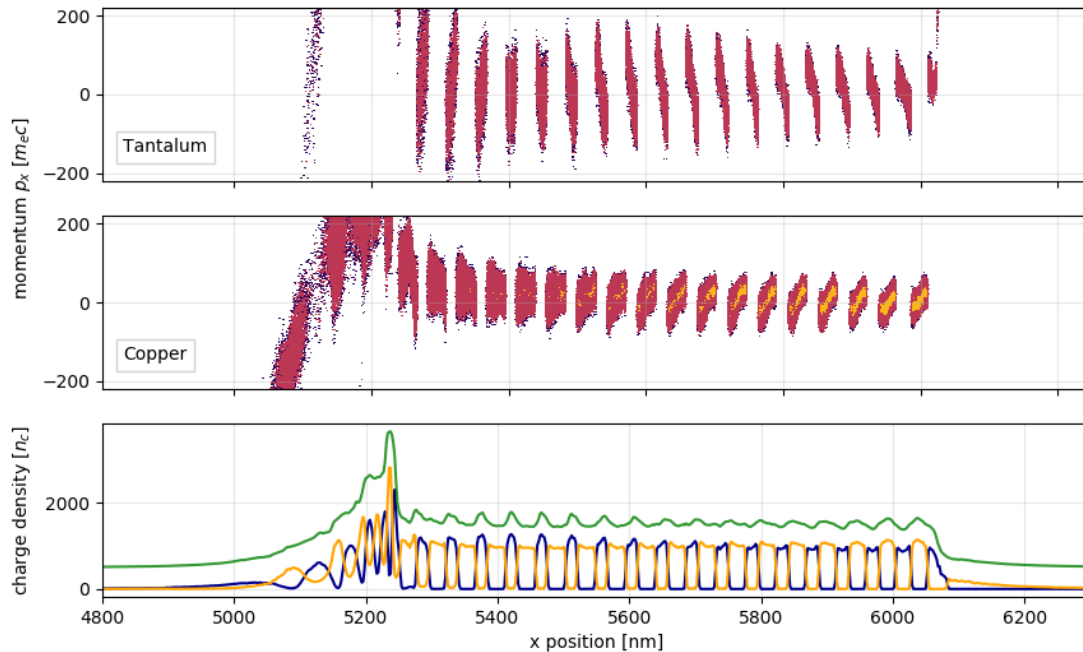
Figure 4.12: Density profile and phase space of ion species and free electrons (green) at t = 125 fs for I = 10^{21} Wcm^{-2} and setup nb.1.

What we learned at this point is, that the density alteration of the ion profile shows a different part of the dynamics than the density alteration of the electron profile. The ion density alteration shows us where the ion charge densities are equal, so the middle region of figure (4.11), the electron density alteration shows us, where the total electron densities are equal, which appears when the copper nitrite layers are the dominant layers, so the front region of figure(4.11). This explains why we see 2 ion density alterations moving through the target, but only one electron density alteration in figure (4.10). The layer relation changes two times, causing two ion density alterations as in figure(4.11), each time when the layers change roles. We start with tantalum as the dominant layer, then copper, then tantalum again. The electron density alteration occurs, when copper nitrite is the dominant layer, so only once. We can further conclude that the electron density alteration will always show half the appearance frequency of the ion density alteration.

Here we can come back to the wave discussion of the density alteration. As explained above, calling it a wave would have been misleading, because we have a row of single, almost independent oscillations, as will be proofed soon. Now we understand that the global density alteration is only a result of that. There is no actual density wave traveling through the target at this time scale. With this knowledge and no further room for misunderstanding the process, we can now define an appearance frequency of the density alteration. The frequency here does not draw back to the wave behaviour, but rather the fact that multiple alterations occur over time, making the determination of a frequency more reasonable than one of a velocity.

4.3.2 Process

To understand what causes the oscillation, one has to take a look at the plasma pressure:

$$P_j = n_j k_B T_j \tag{1}$$

with j = {i, e} for ions and electrons. The dynamics are the result of a simple 1D pressure gradient force $F = -\nabla P$ between layers, with

$$P_{Ta} = P_{iTa} + P_{eTa}$$
$$P_{Cu_3N} = P_{iCu_3N} + P_{eCu_3N} \tag{2}$$

taking each ions and electrons in the layer into consideration. Due to tantalum initially having a higher electron density, these layers have higher pressure and can expand first, compressing the lower electron density and therefore lower pressure copper nitrite layers. When the density gradient reverses due to the compression, the pressure gradient does as well. Therefore the copper nitrite layers start expanding and the tantalum layers experience compression. The layers continuously alternate in their dynamics until the oscillation stops. The damping can be caused by for example the intermixing between the layer materials. This leads to the reduction

of the density gradient, the pressure gradient and therefore the force.

Based on the discussion in 2.2.1 it is expected that one can neglect the pressures of ions P_i in the beginning, due to them gaining energy only after the electrons. Therefore, initially there is $T_i \ll T_e$ and the pressures simplify to $P_{Ta} = P_{eTa}$ and $P_{Cu_3N} = P_{eCu_3N}$. As soon as the ions gain energy, they can not be neglected anymore.

Lets focus on the first times and take only electrons into account. The pressure can only arise if the electrons gain a relevant temperature, but assuming that the electron temperature is quite similar in one target region, meaning layer independent, it does not cause a significant pressure gradient in between the layers. The density however causes a significant gradient, when layer materials are chosen accordingly (Ta - $n_e = 2320n_c$, Cu_3N - $n_e = 870n_c$, when fully ionized).

This finally leads to the assumption that the electron density gradient between the layers is the initial cause of the oscillation. This explains why tantalum is the first dominant layer, it has a lower ion density than copper nitrite, but it's electron density is larger, which results in a larger pressure and the tantalum layers compressing the copper nitrite layers.

The electrons consist of energetic free electrons, created by ionization due to the laser pulse or collisional ionization, and low temperature bound electrons, still moving with the ions. With the same argumentation as above, this leaves the free electrons as the initial cause of the dynamic, because the bound electrons barely carry energy. The division is less relevant for higher intensities, when a target is fully ionized, but may play a role in the lower intensity regime. Final conclusion is that the free electrons drive this oscillation.

Now we learned that the pressure gradient can only arise for free electrons. Initially all electrons are bound, but when the laser hits, the target gets ionized by collisional ionization throughout its lenght, starting at the front. This causes the oscillation dynamic to start at the front and not simultaneously everywhere in the target. The oscillation starts to arise when a layer region is sufficiently ionized and heated. We also assume, that the single layer oscillations are not impacted by the neighboring oscillations, which would make the density alteration a wave. We can proof that by simply by pointing out, that the density oscillation starts again at the front after the first occurrence. If the DO would depend on the pressure of neighboring layers, i.e. pressure that one layer is performing on the next layer and then the next and so on, there would be no second occurrence at the front. The only reason why a second density alteration can occur at the front is because the front layers continue to oscillate on their own and create a new density alteration, which implies that the single layer oscillation is enough to cause the density alteration and effects of neighboring layers are negligible.

4.3.3 Parameter Scan

Observing how the oscillation behaves under diverse conditions, e.g. different laser intensities, supports understanding and physical modeling. Therefore in this section there will be an analysis of the scans over different parameters, starting with the position of the MLs in the target for setup no. 1 for I $= 10^{20}$Wcm^{-2}, we will determine the height and width of the ion density peak that represents one layer in order to characterize it and follow it over time. Here we chose to look at the density, not charge density. Even though the charge density is the initial cause of the oscillation, its profile is also impacted by ionization effects. To see the pure oscillation happening it is more reasonable to look at the number density.
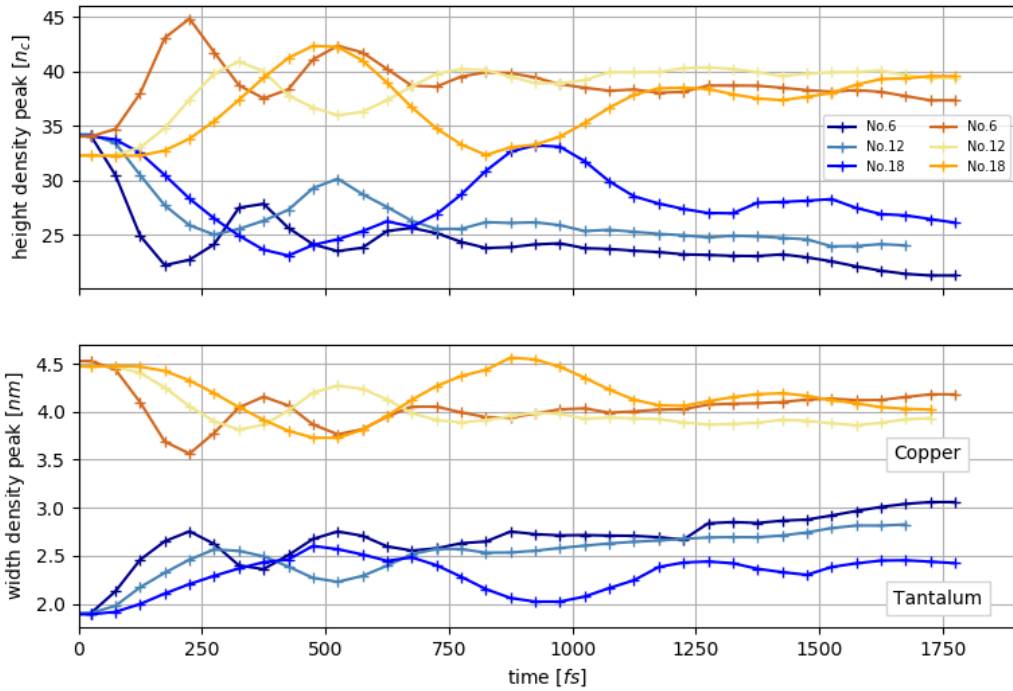
Figure 4.13: Height and width of ion species layer density (tantalum - blue, copper - orange) for 3 layer positions (front, middle, back), I $= 10^{19}$ Wcm^{-2} and setup nb.1.

Figure(4.13) shows time evolution for height and width of the layer, 3 different positions (front, middle, back) and the two materials tantalum(blue) and copper(orange). One can recognize oscillation in height and width, as well as its damping over time. The layers gain in height (decrease in width) when getting compressed and decrease in height (gain in width) when expanding. Furthermore one can detect the phase shift of the oscillation between the front, middle and back layer (layer No. 6, 12 and 18). This points to the dynamic depends on the initial heat diffusion through the target. So the oscillation starts earlier in the front and later in

the back, because the front gains energy first, due to laser impact, the backside later, because of diffusive heating. Remember here, that the pressure gradient can only arise for a significant electron temperature T_e.

Also, the period of the oscillation increases for the rear layers, again because of the heat gradient through the target, see Figure (4.17), causing higher electron temperatures in the front. We can therefore assume that the oscillation period is decreasing for higher energies.

Another observation from figure(4.13) is the inverse movement of the two materials. Both width and height are reversed for neighboring tantalum and copper nitrite layers, compare for example layer no.18 for both materials. This is, in addition to the phase spaces in figure (4.11) and (4.12), another indicator for the oscillation depending onto the reverse behaviours of the layer materials, meaning while one is expanding, the other is getting compressed.
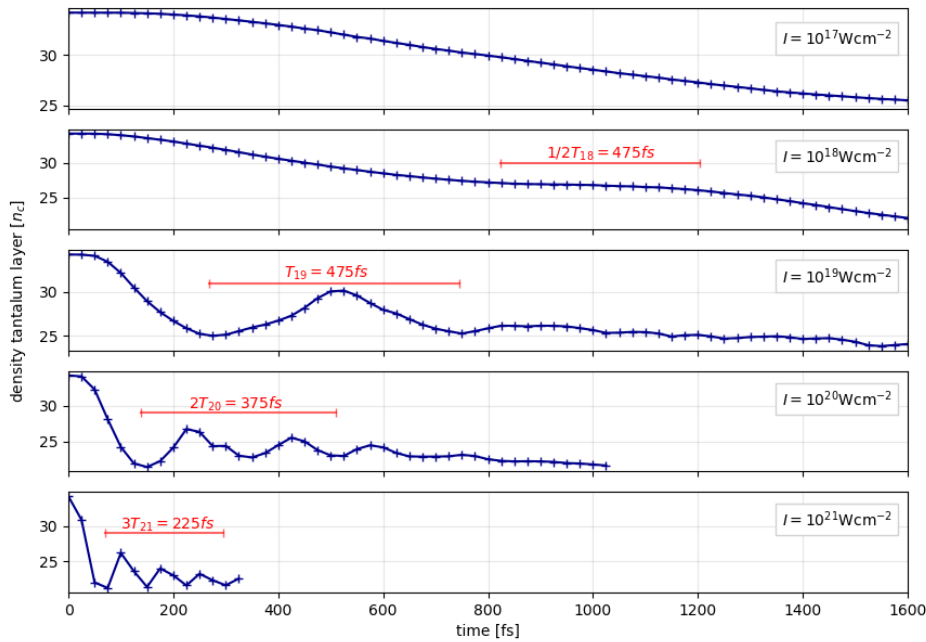
Figure 4.14: **Height of tantalum layer density (middle layer, nb. 12) for intensities**
$I = 10^{17}$-10^{21} Wcm^{-2} and setup nb.1.

In order to better understand the energy dependencies, lets see what impact the laser intensity has. Figure(4.14) shows the time evolution of the middle tantalum layer density for 5 different intensities. For high intensities, the compression of the target destroys the front side, which does not allow to further measure the oscillation.

The comparison shows that the period T_{osc} of the tantalum oscillation decreases with increasing laser intensity. Higher intensities cause higher electron temperatures, increasing the pressure gradient. The expansion happens faster and the reversion of the layer dynamics due to rever-

sed densities occurs earlier, causing the period to decrease. This also explains the increase of oscillation period within the target, that we saw in figure(4.13).

What also seems to increase with energy is the damping. The damping can be defined as the difference in amplitude between the first and following oscillations. It is not initially clear what causes the damping, so it not trivial to explain how it behaves for different energies. Figure (4.14) can be interpreted with mixing. The intermixing of particles and therefore layers, which happens faster for higher energies, causes the pressure gradient to decrease and therefore damps the dynamic. One could also reason as in [28] and assume that the pressure in one layer is different for expansion and compression, even though having constant T_e and n_e. A layer in the bulk wants to expand when heated, due to the thermal motion of the particles, causes energy loss for the compression. Here we realize that further investigation is necessary to fully understand the damping.
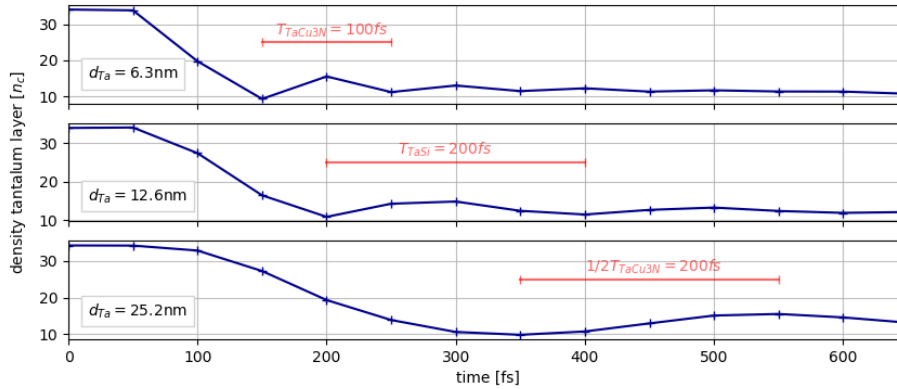
Figure 4.15: Height of tantalum layer density (layer 500nm inside the target) for I $= 10^{20}$ $^{-2}$ and 3 layer thicknesses (simulation setup no.3).

The next parameter to take a look at is the layer width. Figure (4.15) shows the oscillation of the middle tantalum layer for 3 different widths for simulation setup no.3 and I $= 10^{20}$Wcm^{-2}. Middle layer here denotes a layer that stands 500 nm inside the target, not specifically n-th layer because it would have a different position for the 3 setups, resulting in invalid comparisons due to different temperatures. The factor in between the tantalum and copper nitrite layer thicknesses for each 3 cases is $f = d_{Cu_3N}/d_{Ta} = 2.6$.

We can see, that the oscillation period increases with layer thickness. This might seem perplexing at first, since the pressures are not dependent on lyaer width according to formula (2). A thicker layer may have a higher amount of electrons than a thinner one, but the pressure only cares for densities, not absolute particle numbers. However, it is still pretty intuitive, to understand what impact the layer width has. First of all, the thicker a layer, the more it has to be compressed in order to e.g. double its density. Therefore for identical densities, but thicker

layers, the same pressure force has to compress further in order to reach a density, that reverses the pressures, which causes the oscillation period to increase. Secondly, the thicker a layer, the more ions are in the layer. Even though the ions barely play a role in the pressure, they still experience compression and expansion. The heavy ions have to be compressed or expand, the slower the dynamic, the bigger the oscillation period. This easily explains the trend in figure (4.15).

A last relevant parameter scan is the one of electron density difference between the layers. Lets assume in this section that the target gets fully ionized, so we can handle all electrons as relevant free electrons. This assumption is legitimate for an intensity of $I = 10^{20}$ Wcm^{-2}. Figure (4.16) shows the oscillation of the middle tantalum layer (12th) for $I = 10^{20}$ Wcm^{-2} and 3 electron density differences between the layers.
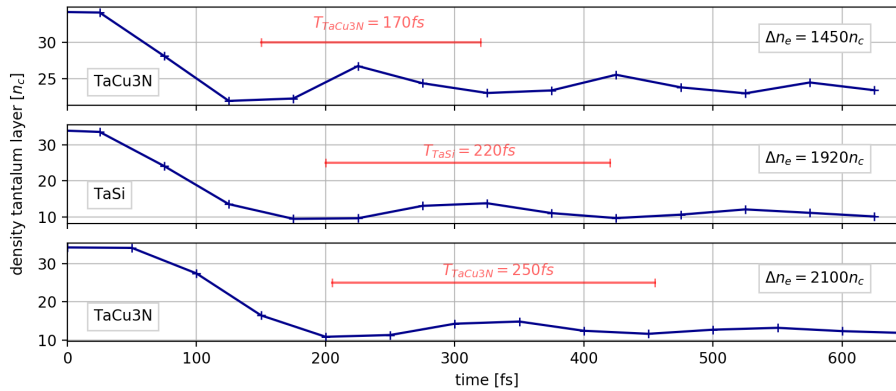
Figure 4.16: Height of tantalum layer density (middle layer, nb. 12) for intensities $I = 10^{20}$ Wcm^{-2} and setup no.1.

The top profile shows simulation setup no.1, so tantalum and copper nitrite ML with an electron density difference of 1450 n_c. The middle profile shows the shows simulation setup no.2, so tantalum and silicon ML with an electron density difference of 1920$_c$. The bottom profile shows simulation setup no.3, so tantalum and copper nitrite ML with an electron density difference of 2100 n_c. When comparing the top and middle profile, one can see an increase of the oscillation period. Even though the pressure force is greater for a higher density difference, the initial recessive layer has to be compressed further in order to overcome the density of the dominant layer. Also, lets not forget that the total density of electrons defines the whole laser-target interaction. Less electrons, as in a TaSi target, lead to a smaller laser absorption and also slower diffusional heating. Therefore the temperature and also the pressure force is lower. Additionally, a change in electron density naturally requires a change in target material. This also changes the ion mass, that also impacts the dynamic, as mentioned above. This reasoning however leads to a smaller oscillation period for TaSi, because the silicon ion is lighter than the copper nitrite ions. In order to eliminate the last factor, we used the simulation of setup no.3. There the density of copper nitrite was set to a quarter of its solid density in order to steepen

the electron density gradient without changing the ion mass. The bottom profile shows the same tendency as the middle one: the oscillation period increases for higher electron density differences, but less total electrons.
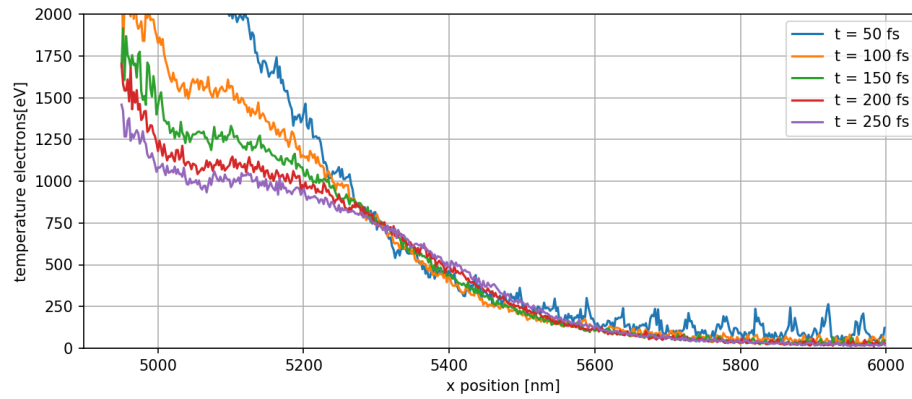
Figure 4.17: Electron temperature gradient through the target for intensity I = 10^{19} **Wcm⁻² and setup no.1.**

4.3.4 Modeling

When modeling the oscillation one can adapt the setup of [28]. The setup consists of two ideal gases in a horizontal cylinder with adiabatic walls, as shown in figure(4.18). The gases are separated by a piston of relevant mass, which is able to move horizontally without friction. Initially the two gases have different pressures and the piston is held in place. As soon as it is freed, the gas with higher pressure expands, compressing the second one, causing it to increase in pressure and inverse the process. This causes an oscillation of the piston.
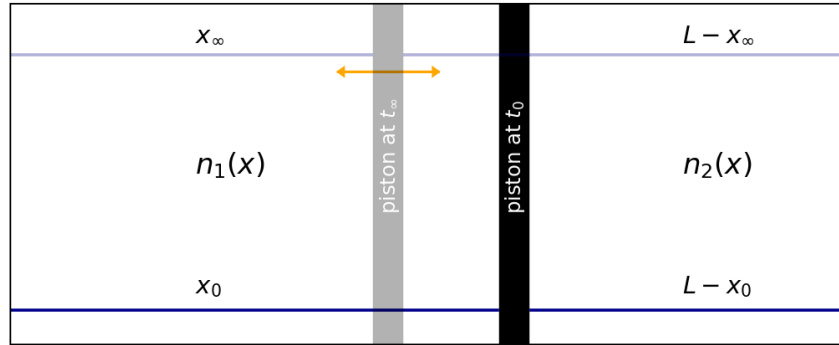
Figure 4.18: Setup gases in horizontal cylinder, as in [28].

Now adapt to our problem and assume the densities in both subsystems to be

$$
\begin{aligned}
n_1(x) &= n_1^0 \frac{x_0}{x(t)} \\
n_2(x) &= n_2^0 \frac{L - x_0}{L - x(t)}
\end{aligned}
\tag{3}
$$

with x_0 and $x(t)$ as the initial and current position of the piston, as well as L being the length of the cylinder. The densities change, depending on how compressed or expanded the chambers are. In addition to that x_∞ denotes the piston position at the end and we set $\Delta x := x - x_\infty$. Now remember the definition of the plasma pressure as in equation (2) and equal it to $P = F/A$, then

$$
\frac{m_p \ddot{x}}{A_p} = P_1 - P_2 = T \left[\frac{n_1^0 x_0}{\Delta x + x_\infty} - \frac{n_2^0 (L - x_0)}{L - \Delta x - x_\infty} \right]
\tag{4}
$$

with the pressures P_i of each subsystem acting on the piston, as well as the piston mass m_p and surface A_p. When adapting the model to the DO dynamics the electrons are considered the ideal gas while the heavy ions are treated as the piston. This draws back to the assumptions from above: the cold ions are not considered in the plasma pressure, thus $n_j^0 = n_{je}^0$. Also, the layer electron temperatures in equation (2) are considered equal, thus $T = T_e$. The piston mass

therefore is

$$m_p = f A_p \frac{x_0}{2} n_{1ion}^0 m_{1ion} + f A_p \frac{L - x_0}{2} n_{2ion}^0 m_{2ion} \equiv f A_p \tilde{m} \tag{5}$$

with m_{jion}, n_{jion} the ions mass and density for each layer, A_p is the piston surface. The factor $1/2$ for the layer widths in (5) considers only half the layer to oscillate, because we assume that the other half oscillates into the other direction. The factor f can correct this estimate by considering even less of the target, we set it to $f = 1/2$. When comparing the copper phase spaces of figure (4.11) and (4.12) we see that for the lower intensity, so (4.11), only the ions at the outer quarter of the layer (f=1/2) show significant momentum. For later times and higher energies, so (4.12), we see that all ions in one half layer (f = 1) are oscillating. We conclude, that the factor f is time depended, but as an estimate we set it constant over time.

Now inserting (5) in (4) and calculating the talyor-series for $\Delta x = 0$ leads to

$$\ddot{x} = -\Delta x \frac{T_e}{f \tilde{m}} \left[n_{1e}^0 \frac{x_0}{x_\infty^2} + n_{2e}^0 \frac{(L - x_0)}{(L - x_\infty)^2} \right] = -\Delta x \omega^2. \tag{6}$$

The approximation $\Delta x = 0$ is applicable because we expect only small deflections around the final position x_∞, as the orange arrow in figure(4.18). The frequency increases with electron temperature, which we already confirmed in the last section in figure(4.14). Also, naturally, the frequency decreases for heavier ions or more ions, as we have seen in figure(4.15). In order to now determine the dependency on the densities and layer thicknesses, we have to find an expression for x_∞. We use the condition $F = 0$ for $n_{1e} = n_{2e}$ and formula (3) to get

$$n_{1e}^0 \frac{x_0}{x_\infty} = n_{2e}^0 \frac{L - x_0}{L - x_\infty} \tag{7}$$

and finally

$$x_\infty = \frac{L}{1 + \frac{n_{2e}^0 (L - x_0)}{n_{1e}^0 x_0}}. \tag{8}$$

We can see that $x_\infty = x_0$ for $L = 2 x_0$ and $n_{1e}^0 = n_{2e}^0$, meaning the piston does not move at all. We also see, that the quotient of the initial densities n_{2e}^0 / n_{1e}^0 plays and equal role as the quotient of the initial widths of the layers $(L - x_0)/x_0$. Lets name this factors and see how x_∞ behaves:

$$\alpha = \frac{n_{2e}^0}{n_{1e}^0}$$
$$\beta = \frac{(L - x_0)}{x_0} \tag{9}$$

Remember at this point, that β is irrelevant for the initial pressure. One can understand that

by setting $\alpha = 1$ and then calculate the initial pressure with (3) for different β. For later times β becomes relevant for the pressure, because we use it to determine the current density. We can also see how β is relevant for ω, because thicker layers cause a higher piston mass and therefore a decrease of the frequency, as discussed above. Nevertheless, initially β is irrelevant as a pure cause of the oscillation.

We will now set $\beta = 2.6$, equivalent to the layer thickness proportions in the simulations. The blue graph in figure(4.19) shows x_∞ for $n_{2e}^0 > n_{1e}^0$ and the orange graphs shows $n_{2e}^0 > n_{1e}^0$. Naturally, the graphs meet at $\alpha = 1$, then $F = 0$ and $x_\infty = x_0$. Here we see how bigger differences in electron density lead to bigger differences in between x_0 and x_∞.
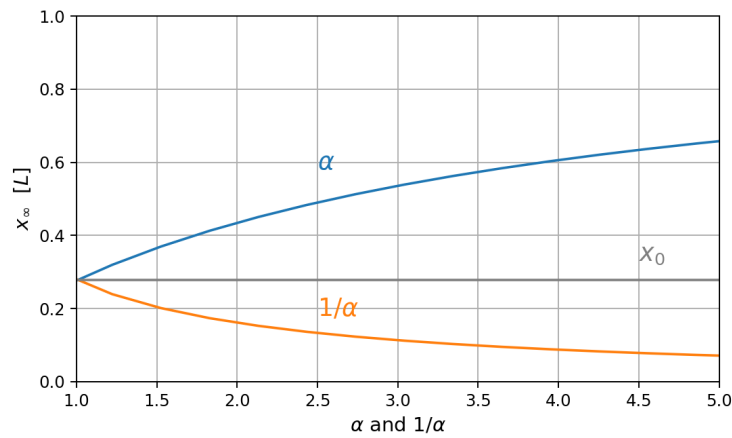
Figure 4.19: Final position of the piston x_∞ for $\beta = 1$.

Now that we understood x_∞, we can look at the frequency ω and period T_{osc} in dependence of the laser and target parameters. Figure(4.20) shows the modeled oscillation period T_{osc} in dependence of the electron energy T_e for 3 different values of f and the oscillation periods of the simulations as in figure (4.14) and (4.13). The electron temperatures were taken at the layer position (front, middle, back) and at the time of the occurrence of the first density maximum of tantalum.

 Figure(4.20) shows, that the simple model and the simulations fairly agree. We can also see, that the factor f has no major impact onto the fit, even though f = 0.7 seems to fit the best. Additionally, figure (4.21) shows the oscillation period modeled for a half and fully ionized target in comparison to the simulations. Again we see, that the parameter does not significantly change the trend, but we find that the model fits best to the fully ionized target.

Finally, we see how the measurement of the oscillation period in an experiment would lead to the electron temperature T_e. We can therefore use the dynamics to determine a value of high interest. Nevertheless, one should further investigate the accuracy of the model, e.g. by considering damping.
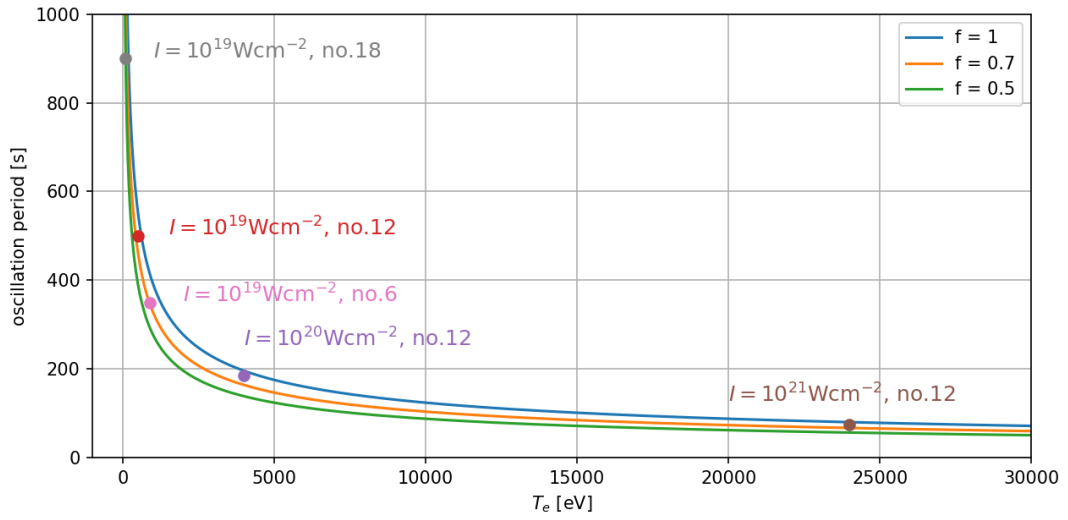
Figure 4.20: Comparison oscillation period T_{osc} for model and simulation.
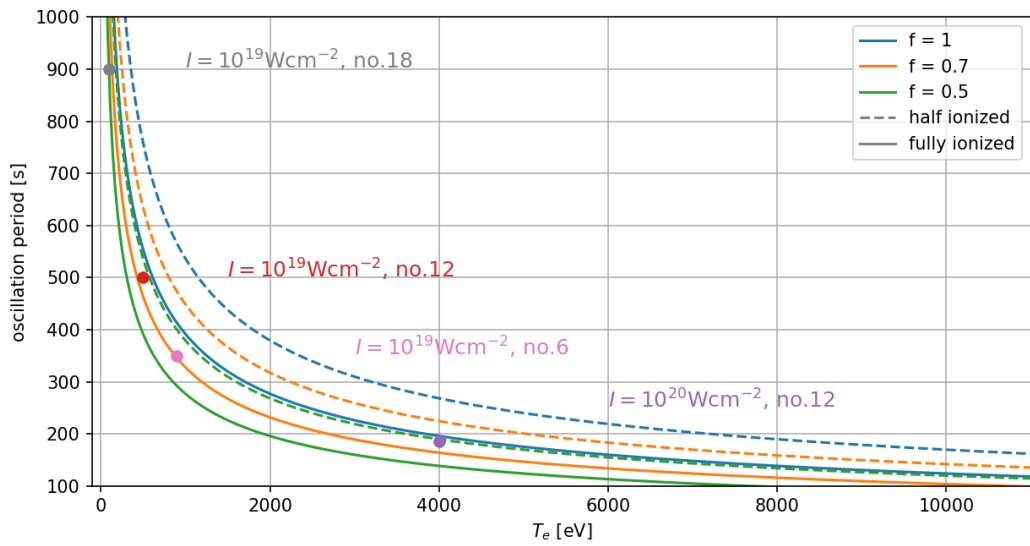
Figure 4.21: Comparison oscillation period T_{osc} for model and simulation for different values f and ionization.

4.3.5 GISAXS Feasability

The final question is: will we see the density oscillation in a GISAXS pattern?

The DO dynamics purely show in the density profile, which already applies them for a GISAXS diagnostic. Now remember the resolution parameters $n_{GISAXS} = 200$ n$_c$ and $t_{GISAXS} = 500$ fs and see, whether we can recognize a pattern.
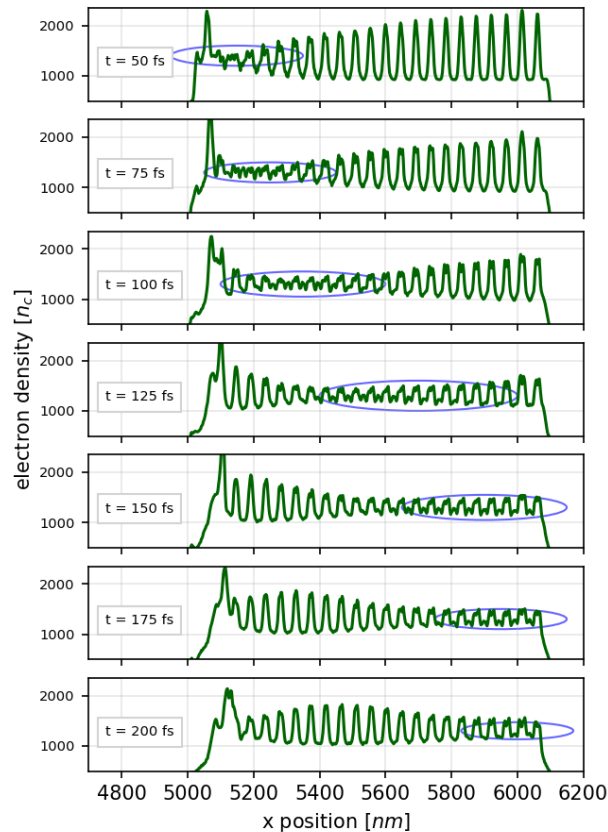
Figure 4.22: Electron profile for I = 10^{20} Wcm^{-2} and setup no. 1.

Lets again take a look at the electron density in figure(4.22). It is to be expected, that the pure oscillation dynamic will not be visible in the pattern, because small increases of peak densities could not be resolved. Therefore we will not see the single layer oscillation. However the density alteration, see figure(4.22), can be recognized. GISAXS is able to locate the first place in the target, where the ML structure shows, when the layer density difference is more than 200 n$_c$. For the cold target, one would be able to see the front ML structure, but as soon as the density alteration appears the scattering pattern would not be able to recognize the peaks anymore and overlook the front. When the density alteration passend and is in the back of the tagret, the ML structure at the front recovers. Then the pattern would once again recognize the front profile. One can now determine over time how often we detect a destroyed

ML front structure and therefore extract the oscillation period T_{osc}.

Remember here, that we measure tantalum in the electron profile, as explained in 4.3.1., but that the oscillation period for both layers is equal, because of the inverse behaviour, as seen in figure(4.13).

Finally, when looking at 4.22, we see, that one needs a time resolution of at least 100 fs to portray the density oscillation. Here we once again refer to mass-limited targets [27] to increase the time resolution, without further explanation. For higher intensities it may become necesssary to rech a timeresolution < 50 fs, as seen in figure(4.14) for I $= 10^{21}$ Wcm^{-2}

5 Conclusion and Outlook

A first realization, that we can take from this work is, that a computational simulation is a useful tool to assist an experiment. We already see in [6], that the collaboration of experiment and simulations leads to a throughout evaluation, because the simulation knows parameters, that the experiment lacks. In this work we learn about simulations as a test implementation of an actual experiment that is planned for the future. The relatively cheap and fast implementation of the simulation allows to predict whether a chosen setup is appropriate for the given physical regime and how it should be modified if not. After the work process of this thesis and amount of insight we got, it is definitely recommended to use simulations as an experimental forecast or to assist an experiment to increase understanding again.

In terms of front- and back side dynamics of the target we learned, that we can not extend the ablation studies of [6] to the high intensity regime, because the target front does not bring an ablation velocity. We can however apply GISAXS at the front for compression and at the rear for TNSA. It is highly recommended to apply GISAXS at the backside of a target in the UHI regime, which has not been done yet. This would allow to portray the TNSA dynamics in a density profile on a femtosecond scale, which has also not been done yet. For these studies one should use a silicon support and place enough ML at the rear side ($\simeq 1\mu$m), no necessity for a pure ML target as in the simulation. The silicon support should be 1-5 μm, depending on the laser intensity regime, because for 10^{17} Wcm^{-2} the target stayed intact, but for 10^{22} Wcm^{-2} one would probably need a thicker target than in this work. The material for the multi layer can be adapted from the simulation setup, but it would also be reasonable to try new layer constitutions, like tantalum and silicon or copper and silicon. This would allow to analyze different ions in the acceleration dynamics. Remember, that we still need an electron density difference between the layers in order to see a ML structure and therefore a GISAXS pattern.

When looking at the density oscillation, the first understanding that we take from this work is how it appears in a density profile. The characteristic density alteration is easy to spot and to understand. We can conclude, that the implementation of targets fully containing ML is very reasonable in order to investigate this dynamic.
The next step should be to use the program BornAgain, mentioned in 2.1, to calculate GISAXS pattern based on the electron density profiles of the simulation to ascertain the rough

estimates of n_{GISAXS}. It should reveal whether the appearance and vanishing of the density alteration is recognizable. If that is not the case, one should either find another ML composition, that promises a more significant ML structure or one has to find another plasma diagnostic to portray the dynamic. Nevertheless, we are confident in the rough estimate of n_{GISAXS} and therefore expect a GISAXS pattern to portray the DO.

The following step would be to ascertain the existence and relevance of the DO dynamics by setting up an experiment according to the simulation setup, i.e. tantalum and copper nitrite targets like for simulation setup nb.1 and apply GISAXS. It is recommended to either use thicker layers or a lower intensity (here 10^{19}-10^{20} Wcm^{-2} are the most suitable to observe the DO dynamics, so it is recommended to apply $\simeq 10^{17}$-10^{18} Wcm^{-2}), because the semi 2D simulation underestimates the diffusion, therefore heating and mixing of the target, as mentioned in 4.1. Because of that we expect faster DO dynamics in 3D and faster vanishing of the ML structure ("smoothing").

Next to the experimental point of view, we also got a decent idea of the theoretical basics of the density oscillation. After understanding how we see it, in the density alteration, and why it occurs, because of the plasma pressure, we saw how the temperature, electron density and layer thickness influences the dynamics in the simulation. This knowledge allows to model the DO according to[28]. The model and simulation showed fair agreement in electron temperature dependency. The next step is to extend the model with a damping mechanism. Here [28] can be used as a reference once again. The extension should once again ensure agreement with the simulations.

We can finally conclude, that GISAXS is feasible for high intensities. The dynamics we see in the pattern differ to the lower intensity regime, but they are not of less interest. For the target setup of this work (no.1) we can see compression, ion acceleration and the density oscillation.

6 Bibliography

[1] B. A. Remington, R. P. Drake, H. Takabe, and D. Arnett, *A review of astrophysics experimentson intense lasers,* Physics of Plasmas 7, 1641–1652 (2000).

[2] S Atzeni, J Meyer-ter-Vehn, *The physics of inertial fusion: beam plasma interaction, hydrodynamics, hot dense matter,* Oxford: Clarendon Press (2004).

[3] Leonhard Karsch, Elke Beyreuther, Wolfgang Enghardt, Malte Gotz, Umar Masood, Ulrich Schramm, Karl Zeil & Jörg Pawelke. *Towards ion beamtherapy based on laser plasma accelerators,* Acta Oncologica, 56:11, 1359-1366, DOI:10.1080/0284186X.2017.1355111(2017).

[4] A.J. Gonsalves, K. Nakamura, J. Daniels, C. Benedetti, C. Pieronek, T.C.H. de Raadt, S. Steinke, J.H. Bin, S.S. Bulanov, J. van Tilborg, C.G.R. Geddes, C.B. Schroeder, Cs. Tóth, E. Esarey, K. Swanson, L. Fan-Chiang, G. Bagdasarov, N. Bobrova, V. Gasilov, G. Korn, P. Sasorov, and W.P. Leemans, *Petawatt Laser Guiding and Electron Beam Acceleration to 8 GeV in a Laser-Heated Capillary Discharge Waveguide,* Phys. Rev. Lett. 122, 084801 (2019).

[5] M. Rehwald, et al., *Laser-driven magnetic-vortex acceleration of protons to 80MeV from density tailored cryogenic hydrogen jets,* in submission (2021).

[6] Lisa Randolph, Mohammadreza Banjafar, Thomas R. Preston, Toshinori Yabuuchi, Mikako Makita, Nicholas P. Dover, Christian Rödel, Sebastian Göde, Yuichi Inubushi, Gerhard Jakob, Johannes Kaa, Akira Kon, James K. Koga, Dmitriy Ksenzov, Takeshi Matsuoka, Mamiko Nishiuchi, Michael Paulus, Frederic Schon, Keiichi Sueda, Yasuhiko Sentoku, Tadashi Togashi, Mehran Vafaee-Khanjani, Michael Bussmann, Thomas E. Cowan, Mathias Kläui, Carsten Fortmann-Grote, Adrian P. Mancuso, Thomas Kluge, Christian Gutt, Motoaki Nakatsutsumi, *Nanoscale subsurface dynamics of solids upon high-intensity laser irradiation observed by femtosecond grazing-incidence x-ray scattering,* arXiv:2012.15076 [physics.plasm-ph] (2020).

[7] P. Müller-Buschbaum, *A Basic Introduction to Grazing Incidence Small-Angle X-Ray Scattering. In: Gomez M., Nogales A., Garcia-Gutierrez M., Ezquerra T. (eds) Applications of Synchrotron Light to Scattering and Diffraction in Materials and Life Sciences. Lecture Notes in Physics,* vol 776. Springer, Berlin, Heidelberg (2009)

[8] G. Pospelov, W. Van Herck, J. Burle, J. M. Carmona Loaiza, C. Durniak, J. M. Fisher, M. Ganeva, D. Yurov and J. Wuttke, *BornAgain: software for simulating and fitting grazing-incidence small-angle scattering,* J. Appl. Cryst., 53, 262-276 (2019)

[9] Sergei I. Anisimov, Baerbel Rethfeld, *Theory of ultrashort laser pulse interaction with a metal* Proceedings Volume 3093, Nonresonant Laser-Matter Interaction (NLMI-9) (1997)

[10] Nicholas, D.J., *The development of fluid codes for the laser compression of plasma* (RL–82-083). United Kingdom (1982)

[11] Lyman Spitzer, Jr. , Richard Härm, *Transport Phenomena in a Completely Ionized Gas* Phys. Rev. 89, 977 (1953)

[12] W. Rozmus, V. T. Tikhonchuk, *Skin effect and interaction of short laser pulses with dense plasmas* Phys. Rev. A 42, 7401 (1990)

[13] B. Bezzerides, S. J. Gitomer, D. W. Forslund, *Randomness, Maxwellian Distributions, and Resonance Absorption* Phys. Rev. Lett. 44, 651 (1980)

[14] Andrea Macchi, Marco Borghesi, and Matteo Passoni, *Ion acceleration by superintense laser-plasma interaction* Rev. Mod. Phys. 85, 751 (2013)

[15] J. Reif, *Basic Physics of Femtosecond Laser Ablation. In: Miotello A., Ossi P. (eds) Laser-Surface Interactions for New Materials Production. Springer Series in Materials Science, vol 130., Basic Physics of Femtosecond Laser Ablation* Springer, Berlin, Heidelberg (2010).

[16] Francis F. Chen, *Introduction to plasma physics and controlled fusion, second edition,* Plenum Press (1974).

[17] M. Zepf, M. Castro-Colin, D. Chambers, S. G. Preston, J. S. Wark, and J. Zhang, *Measurements of the hole boring velocity from Doppler shifted harmonic emission from solid targets,* Physics of Plasmas 3, 3242 (1996).

[18] A. P. L. Robinson, P. Gibbon, M. Zepf, S. Kar, R. G. Evans,C. Bellei, *Relativistically correct hole-boring and ion acceleration by circularly polarized laser pulses,* Plasma Phys. Control. Fusion 51 024004 (2009)

[19] Prof. Paul McKenna, *Laser-driven ion acceleration from ultra-thin foil targets,* `https://www.clf.stfc.ac.uk/Pages/McKenna_UKRI%20XFEL%20HED%20Workshop.pdf` (fetched May 2021)

[20] B. Fryxell, K. Olson, P. Ricker, F. X. Timmes, M. Zingale, D. Q. Lamb, P. MacNeice, R. Rosner, J. W. Truran, and H. Tufo, *FLASH: An Adaptive Mesh Hydrodynamics Code for Modeling Astrophysical Thermonuclear Flashes,* B. Fryxell et al 2000 ApJS 131 273 (2000).

[21] C.K. Birdsall and A.B. Langdon, *Plasma physics via computer simulation,* Taylor& Francis (1991).

[22] J. Derouillat, A. Beck, F. Pérez, T. Vinci, M. Chiaramello, A. Grassi, M. Flé, G. Bouchard, I. Plotnikov, N. Aunai, J. Dargent, C. Riconda, M. Grech, *SMILEI: a collaborative, open-source, multi-purpose particle-in-cell code for plasma simulation,* arXiv:1702.05128 [physics.plasm-ph] (2017).

[23] Paul Gibbon, *Short Pulse Laser Interactions with Matter,* Imperial College Press (2005).

[24] D.H. Sharp, *An overview of Rayleigh-Taylor instability,* Physica D: Nonlinear Phenomena, Volume 12, Issue 1, p. 3,IN1,11-10,IN10,18 (1984).

[25] T. Kluge, J. Metzkes, K. Zeil, M. Bussmann, U. Schramm, and T. E. Cowan, *Two surface plasmon decay of plasma oscillations,* Physics of Plasmas 22, 064502 (2015).

[26] P.Mora, *Plasma Expansion into a Vacuum,* Phys. Rev. Lett. 90, 185002 (2003).

[27] T. Kluge, W. Enghardt, S. D. Kraft, U. Schramm, K. Zeil, T. E. Cowan, and M. Bussmann, *Enhanced laser ion acceleration from mass-limited foils ,* Physics of Plasmas 17, 123103 (2010).

[28] Eric A. Gislason, *A close examination of the motion of an adiabatic piston,* American Journal of Physics 78(10):995-1001, DOI:10.1119/1.3480028 (2010).

Erklärung

Hiermit erkläre ich, dass ich diese Arbeit im Rahmen der Betreuung am Institut für Kern- und Teilchenphysik ohne unzulässige Hilfe Dritter verfasst und alle Quellen als solche gekennzeichnet habe.

Franziska-Luise Paschke-Brühl

Dresden, Juli 2021